THERMO-MECHANICAL PROCESSING OF AUSTENITIC STEEL TO MITIGATE SURFACE RELATED DEGRADATION

by

Yaakov (Jonathan) Idell

B.S., Nuclear Engineering Technologies, Excelsior College, 2009

Submitted to the Graduate Faculty of

the Swanson School of Engineering in partial fulfillment

of the requirements for the degree of

Doctor of Philosophy in Materials Science and Engineering

University of Pittsburgh

2014

THERMO-MECHANICAL PROCESSING OF AUSTENITIC STEEL TO MITIGATE SURFACE RELATED DEGRADATION

Yaakov (Jonathan) Idell, PhD

University of Pittsburgh, 2014

Thermo-mechanical processing plays an important role in materials property optimization through microstructure modification, required by demanding modern materials applications. Due to the critical role of austenitic stainless steels, such as 316L, as structural components in harsh environments, e.g. in nuclear power plants, improved degradation resistance is desirable. A novel two-dimensional plane strain machining process has shown promise achieving significant grain size refinement through severe plastic deformation (SPD) and imparting large strains in the surface and subsurface regions of the substrate in various metals and alloys. The deformation process creates a heavily deformed 20 ï30 micron thick nanocrystalline surface layer with increased hardness and minimal martensite formation. Post-deformation processing annealing treatments have been applied to assess stability of the refined scale microstructures and the potential for obtaining grain boundary engineered microstructures with increased fraction of low-energy grain boundaries and altered grain boundary network structure. Varying the deformation and heat treatment process parameters, allows for development of a full understanding of the nanocrystalline layer and cross-section of the surface substrate created. Micro-characterization was performed using hardness measurements, magnetometry, x-ray diffraction, scanning and transmission electron microscopy to assess property and microstructural changes. This study provides a fundamental understanding of two-dimensional plane strain machining as a thermo-mechanical processing technique, which may in the future deliver capabilities for creating grain

boundary engineered surface modified components, typified by a combination of grain refinement with improved grain boundary network interconnectivity attributes suitable for use in harsh environments, such as those in commercial nuclear power plants where improved resistance to irradiation stress corrosion cracking is desirable.

TABLE OF CONTENTS

LIST OF TABLES

LIST OF FIGURES

PREFACE

I would like to express my appreciation to all those who made this dissertation possible. Without a doubt, I would not be here without my dissertation adviser, Dr. Jörg M.K. Wiezorek. His guidance, patience, inspiration, and knowledge helped me mature throughout my Ph.D studies. I would also like to Dr. Andreas Kulovits and Dr. Xiahan Sang for their assistance and encouragement through discussion regarding the details of my dissertation. Additionally, I am grateful to Dr. Giovanni Facco, Kai Zweiacker, and Can Liu for providing an exciting and friendly lab atmosphere.

I would like to thank Dr. M. Ravi Shankar and his student Saurabh Basu for their help regarding the theory and use of the 2-D linear plane-strain machining setup.

I am also grateful to the staff in the department of Mechanical Engineering and Materials Science, specifically Albert Stewart and Cole Van Ormer, for their assistance throughout my studies. Also, I am thankful for the financial support throughout my Ph. D studies provided by the Nuclear Regulatory Commission (NRC-38-09-935) and the National Science Foundation (NSF CMMI #0856626).

Lastly, I wish to express gratitude to those close to me who provided support through the trials and tribulation of my Ph.D program. I would not have gotten though my program without the love and support of my parents Bruce and

nah Mayer, for giving me the continued motivation to continue to work hard when frustration set in during my time at the University of Pittsburgh.

ABBREVIATIONS

BCC ïBody centered cubic

BF ïBright field

BSE ïBack-scatter electron

BWR ïBoiling water reactor

CSL ïCoincident site lattice (CSL)

DF ïDark field

DGZ ïDistinguishable grain zone

DPA ïDisplacements per atom

EBSD ïElectron back-scatter diffraction

ECAP ïEqual-channel angular pressing

FCC ïFace centered cubic

FWHM ïFull width at half maximum

GBE ïGrain boundary engineering

GBN ïGrain boundary network

GDX ïGeometric dynamic recrystallization

HAGB ïHigh angle grain boundary

HELP ïHydrogen-enhanced localized plasticity

HPT ïHigh pressure torsion

HSS ïHigh strength steel

IASCC ïIrradiation assisted stress corrosion cracking

IGSCC ïIntergranular stress corrosion cracking

IPF ïInverted pole figure

LPB ïLow plasticity burnishing

LSP ïLaser shot peening

MVF ïMartensite volume fraction

NC ïNanocrystalline

OIM ïOrientation imaging microscopy

PASAD ïProfile analysis of the selected diffraction

PED ïPrecession electron diffraction

PKA ïPrimary knock-on atom

PWR ïPressurized water reactor

RED ïRadiation enhanced diffusion

RIS ïRadiation-induced segregation

SADP ïSelected area diffraction pattern

SCC ïStress corrosion cracking

SE ïSecondary electron

SEM ïScanning electron microscopy

SFE ïStacking fault energy

SIM ïStrain induced martensite

SMAT ïSurface mechanical attrition treatment

SP ïShot penning

SPD ïSevere plastic deformation

TEM ïTransmission electron microscopy

VSM ïVibrating sample magnetometer

XRD ïX-Ray diffraction

1.0 INTRODUCTION

1.1 CURRENT PROBLEMS

Austenitic stainless steels play an important role in the global industry and are widely used in application areas including chemical, paper, energy, transport, and machinery. However, for nuclear power plant reactor environments degradation incidents by intergranular stress corrosion cracking (IGSCC) of highly irradiated internal reactor components, such as the baffle bolts and control rod guide tube split pins, have been reported recently [1, 2]. More specifically, these degradation incidents have been attributed to irradiation assisted stress corrosion cracking (IASCC) [1, 2]. Over the operating lifetime, nuclear power plant reactor core internal components of a pressurized water reactor (PWR) can experience temperatures as high a 400°C, neutron flux at $5.1x10^{13}$ neutrons per cm^2 per s, with energies of E>1.0 MeV, neutron fluence at 40 years of $6.44x10^{22}$ n cm^{-2} (E>1.0 MeV) or on average ~90 displacements per atom (DPA) [3]. In recent years, failures of reactor core internal components have been reported after accumulating fluence as low as 5 x 10^{20} n/cm^2 (E >1 MeV), or ~0.7 DPA, in boiling water reactors (BWR), and at approximately one order of magnitude higher fluences, ~5 x 10^{21} n/cm^2, in some PWR [4]. The fundamental problem of IASCC is linked directly to surface degradation of 316L. Therefore, it is posited here that these degradation challenges presumably can be addressed by improv-

ing the thermodynamic stability and the mechanical strength of the material in the surface or surface near regions of components.

1.2 COMPLEX ISSUES INTRODUCED DUE TO IRRADIATION

Radiation damage occurs by discrete particle-particle interactions through various forms of elastic or inelastic scattering and thermal neutron capture [5]. With enough kinetic energy, a displaced atom, the primary knock-on atom (PKA), will displace other atoms from lattice sites, creating a large number of point defects in a damage cascade. The associated supersaturation of point defects produced under such irradiation conditions eventually leads to genesis of other lattice or crystal defects, such as point defect clusters, dislocations, voids, etc [5]. The sequence of events in irradiation damage starts off with incoming particle, which is either a neutron or high energy gamma ray, (time = 0 seconds) that causes a scattering event displacing the PKA (time = $\sim 10^{-16}$ seconds), which goes to on to displace other atoms from their lattice sites creating a series of series displacements (vacancy and interstitial point defects) known as a displacement cascade (time = $\sim 10^{-14}$ seconds). As the displacement cascade grows, the vacancy and interstitial point defects will recombine in a process known as a cascade collapse (time = $\sim 10^{-12}$ seconds); meanwhile, the point defects that do not recombine will migrate and cluster together (time = $\sim 10^{-9}$ seconds). The clustering of point defects will lead to accumulation of damage in the material (time = $\sim 10^{-6}$ seconds to ~ 10 years) [5, 6]. The irradiation damage results in evolution of the material microstructure and associated property changes. The presence of a high density of intragranular crystal defects (e.g. point defects, point defect clusters, faulted Frank dislocation loops, irradiation induced precipitation) can result in mechanical hardening and loss of fracture tough-

ness of the polycrystalline materials, such as the stainless steels used in reactor internal components. Additionally, as vacancy clusters coalesce, voids are created, which leads to bulk volumetric swelling in the material. The most immediate effect of radiation on metals is radiation-enhanced diffusion (RED), which is an increase in diffusion rate due to the large number of new point defects that are constantly generated in the damage cascades by the high energy irradiation [7]. The RED leads to increased segregation rate at suitable locations within the grains (intragranularly) and at grain boundaries (intergranularly), which are phenomena known as radiation-induced segregation (RIS). The effects of intergranular RIS observed in steels include enrichment of nickel, silicon and phosphorus and depletion of chromium at the grain boundaries relative to the nominal alloy composition [8]. Notably, elemental segregation at grain boundaries has been associated with increased susceptibility to IGSCC for stainless steels [5].

The estimation of depth of radiation damage can be difficult to determine due to several contributing factors, such as neutron energy, length of irradiation exposure, and neutron energy attenuation. When a uranium atom is split, 2.5 neutrons on average are born from this fission reaction. These neutrons are slowed via light water moderation to thermal neutron energy, ~0.025 eV, for continued fission of uranium atoms. Some of the neutrons generated by the fission reactions escape and may cause material damage. The energy of a neutron can be estimated from elastic scattering by using equation (1); where E_f is the final energy, E_i is the initial energy,

n is the number of collisions, and ξ is the average logarithmic energy decrement (for hydrogen,

this value is 1). The number of collisions of the neutron with the hydrogen atom in water to reduce it from fission neutron energy, 2 MeV, to thermal neutron energy is about 19 collisions [9]. The penetration depth of a neutron can be estimated from the neutron mean free path length,

which is the average distance the neutron travels before a scattering interaction occurs. Using equations (4), (5), and (6), the neutron mean free path length can be determined; where σ_i is the microscopic cross section of scattering or absorption, Σ_i is the macroscopic cross section of scattering or absorption, ρ_i is the density of the austenitic steel, N_A is Avogadro's number, λ is the neutron mean free path length. Using the associated microscopic cross sections associated with 316L for a thermal neutron [10], the neutron mean free path is determined as about 8 mm, which would indicate a large depth before irradiation damage would occur and accumulate. There is a thermal neutron energy distribution with 0.025 eV being the most likely energy; therefore, there is a neutron mean free path length distribution with 8 mm being the most likely length. However, for this estimate of 8mm penetration depth, the assumption is that the thermalized neutron immediately enters the stainless steel. This is a poor assumption, as there is some distance between the fuel assembly, where the neutrons are initially produced or óborn ôin the fission process, and the stainless steel reactor internal components. As the neutron travels through the light water of the coolant medium and other condensed matter on its way to the stainless steel component it loses kinetic energy and hence the velocity of the neutron drops off prior to interaction with the stainless steel. There is a relationship of the thermal neutron interaction cross-section with neutron velocity, i.e., $\sigma_T \propto \frac{1}{v}$. Reduced neutron velocity results in larger scattering cross sections and reduced penetration depth and mean free path length. For example, if a fission neutron undergoes 27 collisions, which equates to millimeters of distance as such is the distance between the fuel and baffle assembly, prior to entering the 316L stainless steel, the neutron mean free path length is only 0.098 mm or ~10μm. Additionally, the neutron energy

will be attenuated as it travels through the steel due to the alloying elements as described by equation (3). In equation (3), I is the final intensity, I_o is the initial intensity, μ is the linear coefficient of absorption, and x is the thickness traveled. The majority of the irradiation damage occurs near the surface of the material, which leads to potential voids and RIS near the surface significantly enhancing susceptibility to IGSCC. The radiological dissociation of water into OH^- and H^+ creates additional corrosively active agents to attack potentially susceptible surface sites weakened by irradiation and stress effects. Therefore an investigation into methods to improve surface degradation from irradiation effects, where the majority of the damage occurs, appears warranted.

$$v = 1.383 \times 10^7 \times \sqrt{E} \quad (1)$$

$$E_f = \frac{E_i}{e^{n\xi}} \quad (2)$$

$$I = I_o e^{-\mu x} \quad (3)$$

$$N_i = \frac{\rho_i N_A}{M_i} \quad (4)$$

$$\Sigma_T = \Sigma_A + \Sigma_S = N_i \sigma_{A,i} + N_i \sigma_{S,i} \quad (5)$$

$$\lambda = \frac{1}{\Sigma_T} \quad (6)$$

$$\sigma_T \propto \frac{1}{v} \quad (7)$$

1.3 GRAIN BOUNDARY DESIGN AND CONTROL

IGSCC resistance has been reported to depend on the nature of the grain boundary [11]. The concept of "grain boundary design and control" has been previously introduced, where the bulk properties of materials could be improved by controlling the grain boundary nature [12]. A method of describing the grain boundary structure is through the coincident site lattice (CSL) model [13]. According to the CSL model, the number of coincident sites of the lattices from adjacent grains in the boundary plane gives a measure of the degree of coincidence, which is related to excess free energy of the internal interface, i.e., the grain boundary energy. For example, increasing the number of coincident lattice sites, the degree of coincidence, corresponds to a reduction in grain boundary energy. Grain boundary segments that can be described by this framework, so called low energy CSL boundaries, typically exhibit significantly reduced grain boundary energy relative to grain boundary segments of a more random structure for which less than one percent of lattice sites coincide. These latter high-energy boundaries can be referred to as random or general high-angle grain boundaries. Within the CSL framework the special boundary structures are described by the sigma-N notation, Σ_N, where N is an integer and describes the inverse of the number of lattice sites coincident per unit area of the grain boundary segment. A Σ_3 CSL boundary would entail a grain boundary segment where every third lattice site coincides for the two adjoining grains either side of the boundary. An increased fraction of low energy CSL grain boundaries may improve specific properties of polycrystalline materials. Thus, low number CSL boundaries Σ_N with $N \leq 29$, have been associated with high resistance to sliding, reduced creep rate, and enhanced IGSCC resistance [14, 15]. The most common low energy CSL boundaries are deformation induced or annealing induced twins, also

known as Σ_3 CSL grain boundary. Twin formation is common, especially in face-centered cubic (FCC) alloys with low stacking fault energy (SFE). Low SFE in FCC alloys potentially reduces ductility and may promote premature failure. FCC metals with a wide stacking faults (low SFE) strain-harden more rapidly, twin easily on annealing, and show a different temperature dependence of flow stress than metals with narrow stacking faults, i.e., those with a high SFE. Metals with high SFE exhibit a deformation substructure comprised of dislocation tangles and cells, while low SFE metals show a deformation substructure of banded linear arrays of dislocations [16]. Deformation twins are formed in FCC metals by motion of dissociated unit dislocations, i.e., when a perfect dislocation separates into two Shockley partials separated by a layer or ribbon of stacking fault. The width of the stacking fault is determined by the balance between repulsive force between the two partial dislocations and the attractive force deriving from the surface tension of the stacking fault [17]. Austenitic stainless steels such as 316L are FCC alloys and have a low to intermediate SFE, which is estimated at 62.95 $\frac{mJ}{m^2}$ using the empirically derived and alloy composition dependent equation (8) [18].

$$\text{SFE}\left(\frac{mj}{m^2}\right) = -53 + 6.2(\%\text{Ni}) + 0.7(\%\text{Cr}) + 3.2(\%\text{Mn}) + 9.3(\%\text{Mo}) \quad (8)$$

Not only is the fraction of low energy CSL grain boundaries, the special grain boundaries, important to IGSCC resistance, but the grain boundary network topology is essential in minimizing intergranular crack propagation. The importance of the grain boundary network topology of random and special grain boundaries has been theoretically modeled using percolation theory [19-24] by treating the crystal grains as being separated by either strong or weak links. Strong links are formed by grain boundary segments with low disorientations, low energy CSL

boundaries, or by triple junctions with atleast two low energy CSL boundaries. Conversely, random or non-low energy CSL boundaries are characterized as weak links. Similarly, triple junctions involving a majority of or only non-CSL boundaries are considered weak links in the GB network. Most models using standard percolation theory assume a random distribution of weak and strong links. However, the distribution of orientations of the grains of a material may deviate from a random distribution, which can be described using a concept known as the texture of polycrystalline materials. Texture has been shown to influence the probabilities of the types of boundaries that can occur in a material, and the distribution of the triple junctions [25]. It has been demonstrated that the length of intergranular stress corrosion cracks is expected to decrease as the special boundary fraction increases [20, 24]. These models describe the importance of network topology. The grain boundary network topology can be changed through grain boundary engineering (GBE), which has the aim of increasing the fraction of special boundaries and also by changing the topology of the associated grain boundary network structures, e.g. by reducing interconnectivity of the weak link segments by introducing more strong link segments of grain boundary. For FCC metals and alloys with intermediate to low SFE this can be accomplished through thermomechanical processing. Cycles of plastic deformation and annealing fragment the network of random grain boundaries, creating a distribution of strong links in the network structure and thereby providing microstructural obstacles to crack propagation.

1.4 SURFACE MODIFICATIONS TECHNIQUES TO ADDRESS CURRENT PROBLEM

Surface modification is a means of applying GBE directly to regions most susceptible to crack propagation. Some of the novel surface modification techniques to perform grain boundary engineering include shot peening (SP), laser shock peening (LSP), and low plasticity burnishing (LPB), surface mechanical attrition treatment (SMAT), and two-dimensional (2-D) linear plane-strain machining.

SP is a surface deformation process in which hard particles repeatedly impact the surface of a component with high kinetic energy, creating surface and subsurface compressive residual stress [26]. Residual stresses are the stresses that remain in the material once the load has been removed [16]. SP is a widely used technique for imparting compressive residual stress, which minimizes crack propagation [25], but also has a few drawbacks, including:

(i) Shot peening intensity is not uniform across the component being peened;

(ii) Compressive residual stress is limited in depth usually not exceeding 0.3 mm in soft metals and less in harder metals;

(iii) Peening process results in a roughened surface, which requires removal before use in wear applications, thereby reducing or eliminating the compressive stress layer [27].

LPB is a type of deep rolling deformation process that imparts minimal plastic deformation (3-5% cold working) while creating deep compressive residual stress in the material [28]. Compressive residual stresses can be imparted to greater than 1 mm in depth. However, the lack of availability of this proprietary process and the associated high costs limit its usefulness.

LSP is a deformation process in which a laser shot strikes a material, and propagates a shock wave through the material creating compressive residual stress. The strain rate from this process can be as high as ~10^7 [29] with minimal cold working (<9%) [30]. However, high costs of the required instrumentation, equipment and trained personnel, together with long processing times and limited availability prevent large-scale adaptation of this process.

SMAT is a technique similar to SP except, (i) balls are not fired directly into the material, but rather controlled by a ultra-sonic frequency vibration generator, (ii) the balls used are smooth and smaller, and (iii) random directional impacts are typical [31-33]. This process creates a grain-refined layer by high strain and strain rate plastic deformation. The major disadvantage of SMAT is the inability to scale the surface modification process without high costs for equipment.

2-D linear plane-strain machining is a surface plastic deformation process involving chip formation from a single pass orthogonal machining related technique [34-36]. This surface deformation process also creates a grain refined layer process that produces strain rates between 10^4 and 10^5, and can be adopted for large scale production, while remaining cost efficient [34]. For example, 2-D linear plane-strain machining could be applied to large sheets for production of a grain-refined layer in a single pass at room temperature relatively rapidly, within seconds. Meanwhile other means of production of nanostructured materials involve special geometries, unique equipment, and long processing time of up to many hours (e.g. in LSP or SMAT) to produce the same grain refined layer. This clearly shows plane-strain machining has potential to produce grain refined layers on materials at far lower costs than other processes. 2-D linear plane-strain machining is the least common and least explored of the surface modification processes and methods. Hence further experimental study of its potential as a surface deformation method for GBE approaches appears indicated.

The grain-refined region produced through 2-D plane-strain machining offers benefits and drawbacks regarding performance related properties of austenitic stainless steels. Because of the high strain and strain rate, formation of strain induced martensite (SIM) is likely to occur along with the significantly reduced grain size, which in combination are expected to increase the hardness [37] and strength [38] of the material. The increased strength will require a higher stress to continue crack propagation, which therefore can be considered a positive attribute of the 2-D plane strain machining modified surfaces. However, the increased martensite content will lower the fracture toughness of the material. In the nuclear reactor internal environment neutron irradiation hardening also further induces embrittlement, which taken together with the martensite would result in increasing crack propagation susceptibility. The reduced grain size significantly increases the number and length of grain boundaries in the material. The increased density of internal interfaces, grain boundaries might be expected to increase the resistance to deleterious irradiation related effects on the properties of the material. Grain boundaries have different atomic configurations and local atomic densities than those of the crystal of the intragranular (grain interior) regions. The internal surfaces, the intergranular boundaries, grain boundaries act as sinks for point defects, especially self-interstitials, generated by the irradiation. The sinks absorb or facilitate annihilation of irradiation induced point defects [5]. Increasing the number density of grain boundaries through grain refinement therefore results in lower point defect concentrations in the material. Decreased point defect concentrations will lower both RED and RIS effects. On the flip side, the increased number of grain boundaries allows for a potentially weaker grain boundary network due to the plastic deformation induced increase in random grain boundaries in it. A balance is required between minimizing RIS effects and creating a grain boundary network topology with large fractions of strong links. The grain refinement to the sub-

microcrystalline or nanometer scale regimes alone would not appear to be sufficient to impart the desired improved resistance to IA degradation of the stainless steel. Additionally, GBE would appear to be required to facilitate formation of a GB network topology with enhanced resistance to degradation in the nuclear reactor internal environment.

1.5 RESEARCH OBJECTIVES

To address the chronic issue of surface degradation, an investigation has been undertaken to advance the current state of the understanding regarding formation of a gradient microstructure in the subsurface regions of 316L austenitic stainless steel that is thermally stable in order to improve degradation resistance relevant for nuclear power applications using 2-D linear plane-strain machining. To gain a full understanding of the deformation technique on the substrate, characterization of the produced chip will be necessary. Analytical methods of transmission electron microscopy (TEM), scanning electron microscopy (SEM), and x-ray diffraction (XRD) will be used to provide statistically significant and representative data sets for analyzing morphological changes to develop microstructural mechanism based understanding of the surface modification process and associated heat treatments. The goal of this research is development of an improved understanding of the deformation evolution as a function of the process parameters, specifically strain rate. This is essential to determine the grain boundary network interconnectivity, and grain refinement, quantity of strain induced martensite, and change in mechanical strength caused by the machining process on the surface substrate. In addition, an understanding of the evolution of the plastically deformed microstructure as function of annealing temperature will need to be developed in an effort to develop optimized grain boundary engineered micro-

structures in the 36L material. By altering the deformation process parameters along with the proper heat treatment the microstructure will change, enabling the tailoring of the material properties for the most desirable performance for its intended application.

2.0 BACKGROUND AND LITERATURE REVIEW

2.1 STRESS CORROSION CRACKING

The requirements for stress corrosion cracking (SCC) to occur are a susceptible metal, a corrosive environment, and sufficient tensile stress to induce SCC. There are three major mechanisms to describe the SCC process: (i) Active path dissolution, (ii) hydrogen embrittlement, and (iii) film induced cleavage [5].

The active path dissolution process involves accelerated corrosion along a path in the microstructure with higher than normal corrosion susceptibility, the active path, with the bulk of the material typically being passive. The most common active paths in a typically polycrystalline aggregate used in engineering applications are the grain boundaries. Especially in alloys, where segregation of impurity elements can make passivation of certain grain boundaries marginally more difficult, such active paths can develop [5]. For example, when an austenitic stainless steel has been sensitized by precipitation of chromium carbide along the grain boundary, the local chromium concentration at the grain boundary and in the grain interiors in the vicinity of the carbide precipitate will be reduced. This process can occur in the absence of stress, giving rise to intergranular corrosion that is uniformly distributed over the specimen [39]. The effect of the applied stress is mainly to open up the cracks initiated along the active path, thereby allowing en-

hanced transport of corrosion products away from the crack tip and facilitating faster corrosion of the crack tip [40].

The second mechanism is hydrogen embrittlement. Hydrogen dissolves in all metals to at least a moderate extent. Because of its small size, it is an interstitial atom in the crystals of the metal. Consequently it can diffuse much more rapidly than larger atoms through the lattice and along grain boundaries. Hydrogen tends to be attracted to regions of high triaxial tensile stress where the metal crystal lattice structure is dilated [41]. Thus, it is drawn to the regions ahead of cracks or notches that are under stress. The dissolved hydrogen then assists in the fracture of the metal by making cleavage easier and by assisting in the development of intense local plastic deformation [42]. These effects lead to embrittlement of the metal, which can be explained by the hydrogen-enhanced localized plasticity (HELP) mechanism model [43]. Proposed by Beachem [44], the HELP mechanism is based on the enhanced mobility, increased dislocation velocity for a given applied stress, of dislocations due to enhanced plasticity at the crack tip in the presence of hydrogen atoms. The shielding of elastic fields of the dislocations by the hydrogen atoms causes increased dislocation velocity. This allows dislocations to move along the glide plane more easily and assists in overcoming slip barriers. The local accumulation of dislocations from the enhanced mobility can lead to establishment of soft channels in the grains ahead of the cracks potentially leading to cracking that may be either intergranular or transgranular. Crack growth rates are typically rapid, up to 1 mm/s in the most extreme cases [45]. The BCC crystal structure of ferritic iron has relatively small holes between the metal atoms, but the channels between these holes are relatively wide. Consequently, hydrogen has a relatively low solubility in ferritic iron, but a relatively high diffusion coefficient. In contrast, the holes in the FCC austenite lattice are larger, but the channels between them are smaller. So, austenitic and FCC materials, such as

austenitic stainless steel, have a higher hydrogen solubility and a lower hydrogen diffusion coefficient than BCC ferrite [41]. Consequently, it usually takes very much longer (years rather than days) for austenitic materials to become embrittled by hydrogen diffusing in from the surface than it does for ferritic materials. Therefore, austenitic alloys are often regarded as immune to embrittlement from the effects of hydrogen [41].

The third major mechanism of SCC is film-induced cleavage. If a normally ductile material is coated with a brittle film, then a crack initiated in that film can propagate into the ductile material for a small distance (around 1 μm) before being arrested by ductile blunting [45]. If the brittle film has been formed by a corrosion process then it can reform on the blunted crack tip and the process can be repeated. The brittle films that are best-established as causing film-induced cleavage are de-alloyed layers such as in brass. With brass, it has been shown to fracture on the cleavage plane leading to discontinuous crack propagation in a distinct cleavage pattern (river pattern and ledges), this can result in transgranular fracture [46]. However, gold alloys have been shown to crack intergranularly [47], leading to the conclusion that the type of dominant fracture mode during film-induced cleavage based SCC is dependent on the material.

2.2 INTERGRANULAR STRESS CORROSION CRACKING PRE-REQUISITES

Three factors that will lead to IGSCC include:

(i) Active corrosion by the aggressive environment, which coupled with incomplete passivation of the material, will leave localized regions for accelerated and preferential attack;

(ii) Material deformation leading to both matrix hardening and localized rupture of the oxide film;

(iii) Local deformation under triaxial state of stress results in a stress concentration allowing for transport of ionic species in the aqueous environment into the stressed region [48].

In thermally sensitized austenitic stainless steels, such as the 304- and 316-grades used in reactor internal components, the formation of chromium-rich intergranular carbide, $M_{23}C_6$, results in significant depletion of chromium at significant segments of grain boundaries [49]. This depletion can result in either the complete loss of the protective passive film, resulting in active path corrosion, or a less protective film, which can be easily disrupted by deformation [50]. Both of these processes will result in localized grain boundary attack leading to IGSCC.

2.3 EFFECT OF STRESS ON INTERGRANULAR STRESS CORROSION CRACKING

Another factor to consider in IGSCC is the applied stress. Below a threshold stress, crack growth rate is so low that failure is considered improbable [51]. All engineering components will typically contain defects, such as notches, sharp changes in section, and welds that will produce a local stress concentration. Locally, the stress concentration may exceed the threshold stress even though the nominal stress is below the threshold stress. Additionally, residual stresses produced by welding or deformation may be close to the yield stress [52]. Fracture mechanics takes these defects into account [16] by determining the rate of growth of a pre-existing crack, which is measured as a function of the stress intensity factor at the tip of the crack [51].

The minimum stress intensity factor at which crack propagation occurs is referred to as the threshold stress intensity factor for stress corrosion crack growth in mode I plane strain loading, K_{ISCC}. For a stress intensity above K_{ISCC} the crack growth rate increases rapidly. However, there is a limiting rate known as the plateau crack growth rate or velocity [51, 53]. As the stress intensity factor continues to increase, the crack growth rate eventually begins to increase again as the stress intensity factor approaches the critical stress intensity factor for fast fracture, K_{IC} [53]. Management of the K_{ISCC} is key in approaches to maximizing component and material lifetime. By maintaining the stress and maximum defect size to a stress intensity factor below K_{ISCC}, crack growth and stress corrosion failure can be avoided [45]. Another factor to consider with the stress effects on IGSCC is the decreasing percentage of chromium protecting the grain boundaries, which is essential where RIS affects the material. Previously, it has been shown in slow strain rate testing of thermally-sensitized type 304 stainless steel that the percentage of intergranular cracking increases rapidly as grain boundary chromium levels decrease below a critical level. The critical value can be as high as 16 wt% Cr at sufficiently low strain rates [54]. Even in the case where the local stress concentration at the crack tip is well below K_{ISCC}, RIS can lower the chromium concentration at the grain boundary, potentially allowing crack propagation to occur.

2.4 IRRADIATION ASSISTED STRESS CORROSION CRACKING PREREQUISITES

Once ionizing radiation is introduced, the necessary conditions for IGSCC are altered. The factors for IASCC to occur are ionizing radiation, susceptible material, tensile stress, and a

corrosive environment as shown in Figure 1**.** Irradiation alters the material by elemental redistribution through RIS and may damage the passive film causing the material to be more susceptible to IGSCC. As the material is irradiated, the response to stress is altered to due effects of neutron embrittlement, irradiation climb, and slip localization. Additionally, ionizing radiation changes the activity of the aqueous environment through radiolysis by producing radicals and molecules such as H^+, OH^-, and H_2O_2. Radiolysis is caused by both neutron and gamma radiations. Typically, gamma radiation reduces how aggressive the aqueous environment is through the recombination of radicals and activated complexes [55]. Neutrons are more efficient at forming radicals with little to no recombination due to their higher energy transfer rate. Therefore, neutrons tend to dominate the radiolysis process creating a more aggressive aqueous environment [56]. The aggressiveness of the aqueous environment is not only determined by amount of irradiation, but also by temperature, pressure, presence of dissolved solutes and gases, activity, and pH. As the factors are altered, it is directly related to changes in electrochemical corrosion potential. Andresen [57] has shown high electrochemical corrosion potentials and an associated sensitivity of the crack growth rate as a result of neutron-induced radiolysis products, specifically hydrogen peroxide, H_2O_2. To combat this issue, the nuclear industry has implemented hydrogen water chemistry management strategies to minimize IASCC. Hydrogen is injected directly into the coolant and combines with dissolved oxygen. This lowers the electrochemical corrosion potential of the coolant, thereby mitigating against the detrimental effects from neutron induced radiolysis. Additionally, introducing noble metals, such as palladium, as a minor alloy addition (<1 wt%) attracts the dissolved oxygen minimizing the required hydrogen required to lower the electrochemical corrosion potential [58].

produce additional deformation that is applied onto the chip. The plastic zone ahead of the tool edge is referred to as the primary zone of deformation, and the deformation zone on the rake face is usually referred to as the secondary zone of deformation [59]. Both the primary and secondary zones of deformation will produce heat that will increase the temperature of the materials and interfaces involved in the deformation process. The effective magnitude of the primary deformation zone is dependent on the rake angle (α), cutting speed (v), material characteristics, and frictional heat produced. Material characteristics that affect the primary deformation zone are dependent on strength, strain hardening, strain rate ($\dot{\gamma}$), and heat conductivity [59]. Typical results show that large rake angle tools produce less overall deformation; meanwhile, small or negative rake angle tools, produce a significant deformation [34, 60]. The primary deformation zone produces a highly concentrated shear zone, referred to in the ideal case as the shear plane with little or no compression. The average shear strain (γ) and $\dot{\gamma}$ imposed in the chip can be estimated using equations (9) and (10) [61, 62].

$$\gamma = \frac{\cos(\alpha)}{\sin(\phi)\cos(\phi-\alpha)} \qquad (9)$$

$$\dot{\gamma} = \frac{\gamma}{a_0} \, v \cos\phi \qquad (10)$$

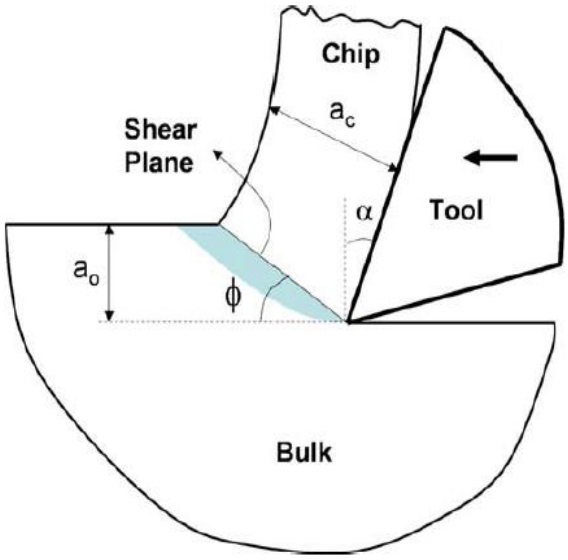

Figure 2: 2-D linear plane-strain machining schematic

Where the shear angle (ϕ) is calculated from a measurement of a_o and a_c (deformed chip thickness) as shown in equation (11).

$$\tan\phi = \frac{\frac{a_o}{a_c}\cos(\alpha)}{1-\frac{a_o}{a_c}\sin(\alpha)} \qquad (11)$$

Hence, regarding the treatment of the strain, strain rate and temperatures arising during the 2-D plane strain machining process the resulting chip is reasonably well characterized from a theoretical point of view. Experimental data available on effective strain, associated strain rates and temperature field developments for the chip produced during the 2-D plane strain machining generally confirms predictions from the theoretical treatments. Unfortunately, theoretical treatments for the effects on the surface and near-surface region, sub-surface regions of the bulk substrates exposed to the plastic deformation and thermal cycles associated with 2-D plane strain machining have not been developed to the same level of confidence and sophistication as for the

chip. Thus significant uncertainty remains regarding the stress/strain states, nature of deformations and thermal exposures for the bulk substrate surface and sub-surface region.

2.6 COMMON SEVERE PLASTIC DEFORMATION TECHNIQUES

Severe plastic deformation (SPD) is a generic term describing plastic deformation processing techniques involving very large strains, which are imposed without significantly altering the geometry of the work piece [63]. When the material is deformed where the geometry is preserved, the free flow of material is prevented, producing significant hydrostatic pressure, which leads to high densities of crystal lattice defects. Two principle techniques for producing severe plastic deformation (SPD) is equal-channel angular pressing (ECAP) and high-pressure torsion (HPT). ECAP is a process where a die containing two channels, equal in cross-section intersecting at an angle that is generally close to 90 degree, are utilized to press a sample through the die using a plunger. This processing was first used in the Soviet Union about 30 years ago [64], and it is recognized that this processing leads to very substantial grain refinement in the material [65, 66]. The strain imposed on the sample processed through ECAP is dependent upon both the channel angle between the two channels. A higher strain is imposed the closer to 90 degrees the angle of intersection is [67]. For a perfectly conforming work piece and an angle of 90° one through the die imparts a strain equivalent of unity. Since the cross-sectional dimensions of the sample remain unchanged on passage through the die, repetitive pressing may be used to attain very high strains in total during multiple pass processing by ECAP.

The SPD procedure of HPT involves a sample in the form of a disk, which is held under a high pressure, and then subjected to torsional straining [68]. Both ECAP and HPT processing

have two advantages of producing exceptionally small grains sizes, often in the nanometer range (<100 nm), and of providing a capability for processing brittle materials such as intermetallics and semiconductors [69, 70]. The major disadvantage of these techniques is that the specimen dimensions are confined based on the size of the apparatus and multiple passes may be required to apply SPD to the material. Even though these techniques are not ideal for producing a thermally stable layer as the SPD is observed throughout the entire material, these methods can serve as a precedent or benchmark for SPD when characterizing the microstructures produced by the 2-D linear plane strain machining.

2.7 HEAT TREATMENT

There are three different stages of in the response to annealing type heat treatments depending on the temperature applied to the plastic deformation processed material, namely, recovery, recrystallization and grain growth. The recovery stage or simply recovery includes processes in which the stored strain or energy is reduced in the deformed grains through the vacancy and point defect mobility related rearrangement of dislocations or removal through the absorption of the point defects and dislocations by the grain boundaries [71]. During this process, high angle grain boundaries (HAGBs) do not migrate, the grain size is not significantly altered and the primary changes in the microstructure are the reduction of the stored strain and the dislocation density. The recrystallization stage, recrystallization, is defined as the set of processes associated with strain-free grains of low dislocation density replacing deformed grains with much higher dislocation density [72]. Typically, recrystallization is associated with a change in texture of the polycrystalline aggregate. The driving force for recrystallization processes is the stored strain

energy in the grain boundaries and in the deformed grains, the dislocation content, leading to migration of the HAGBs. Grain growth, the third stage in the annealing response of cold-deformed metals and alloys, is the process that takes place when the driving force of recovery and recrystallization, reduction of stored energy, is less than the driving force of grain growth, which is derived chiefly from reduction of excess free energy via reduction of total area of grain boundaries [71]. To reduce the total area of grain boundaries, a grain grows and consumes other grains to reduce the number of grains and therefore grain boundaries per volume of material, lowering the overall excess free energy of the polycrystalline aggregate.

Research on severe plastic deformation (SPD) of metals and alloys has suggested that dynamic recovery and recrystallization may occur during the deformation processing of the material [37, 73, 74]. Due to the temperature rise in the material from the deformation process, notably the majority of the mechanical strain energy associated with the plastic deformation strain is converted to heat during cold deformation, recovery and recrystallization processes will annihilate dislocation by driving them to the grain boundaries and convert the low angle grain boundaries of the subgrains into HAGB of newly nucleated stress-free grains. Thus enormous grain refinement can be accomplished by SPD processing. These new smaller stress-free grains constitute the microstructure of the heavily grain refined polycrystalline aggregate after SPD processing and are responsible for the mechanical behavior and other properties, such as the increase in strength. The dislocation bow-out model describes the pinning behavior of these smaller grains on the mobility and glide activation of dislocations during plastic yielding and flow [74]. The plastic yielding occurs in this model when the dislocation configuration reaches a semi-circle at the critical stress. After yielding, the dislocation will tend to create a dislocation loop around the grain known as an Orowan loop making subsequent dislocation motion in the

same glide plane by another dislocation more difficult [17]. However, the dislocation could also become incorporated into the grain boundary under appropriate circumstances, thereby altering the grain boundary structure of the SPD microstructure. This process affects the strain rate sensitivity, which has a direct effect on flow stress leading to an effect on creep rates. The strain rate sensitivity exponent m is defined in equation (12),

$$m \equiv \left(\frac{\partial \ln \sigma}{\partial \ln \dot{\varepsilon}}\right)_T = \frac{1}{\sigma}\left(\frac{\partial \sigma}{\partial \ln \dot{\varepsilon}}\right)_T \quad (12)$$

where σ is the flow stress, $\dot{\epsilon}$ is the strain rate, and T is the temperature. Typical values of m at gran sizes $d = 20 - 80\ nm$ are $m = 0.004 - 0.006$ for BCC Fe [75]. These values are an order of magnitude smaller than for microcrystalline grain sizes in stainless steel, in which $m = 0.04$ [75]. Nanocrystalline grain refinement has a completely different response to changes in the strain rate sensitivity exponent than micron and submicron grain refinement processes, such as conventional cold rolling. In these techniques, the typical trend is the strain rate sensitivity exponent increases as grain size decreases [16]. Since the strain rate sensitivity exponent values for nanocrystalline grain refinement techniques are too small for grain-boundary sliding ($m = 0.5$) or coble creep ($m = 1$) [76], these grain boundary related creep phenomena are unlikely to occur in 2-D linear plane strain machining unless the strain rate is very small and/or temperature is relatively high [77, 78]. As mentioned previously, nuclear power plant applications can experience temperatures as high as 340°C. This temperature corresponds to about $0.37T_M$ for austenitic stainless steel with T_M~1673K. Because m increases exponentially with

respect to flow stress as temperatures increases, this creates a significant difference in creep behavior between different grain sizes. For a given temperature rise, the nanocrystalline grains are more likely to be thermally stable. Necking and the eventual failure due to creep would occur first in the microcrystalline grain sized stainless steel. Hence, some unexpected behaviors and performance related property combinations are predicted to derive from grain size refinements to the nanocrystalline (NC) scale in the 316L. Evidence for establishing NC microstructures in 316L chips and also in narrow surface layers of bulk substrates after SPD by 2-D plane strain machining has been reported recently [37, 79]. Detailed evaluation of the thermal stability and property assessment remains to be performed for the NC 316L derived by 2-D plane strain machining.

3.0 METHODOLOGY

3.1 MATERIAL SELECTION

The majority of the reactor internal components are composed of austenitic stainless steel, specifically 304 or 316L. With the higher molybdenum content, 316L stainless steel, which is a low carbon chromium-nickel austenitic stainless steel, is considered to have superior corrosion and pitting resistance than 304. General applications of 316L include applications requiring high formability, creep resistance, corrosion resistance, and high tensile strength. Due to the high importance of this alloy in the nuclear power and other industries, 316L was selected for this research. 316L austenitic stainless steel plates is commercially available in a hot rolled state from McMaster-Carr with the dimensions of 12ò x 12ò received. Table 1 lists the nominal elemental composition specifications for 316L. Notably, with respect to the ordinary 316-grade the carbon content of the 316L-grade steel is reduced from 0.08 to 0.03wt%. This reduced carbon content renders 316L-grade less susceptible to significant grain boundary carbide formation. However the 0.03wt% C exceeds the solid solubility in the austenitic Fe-Cr-Ni phase and given sufficient time and kinetic factors precipitation of carbides should be expected [80].

Table 1 - AISI Standard Composition for 316L in weight percent (wt.%)

C	Mn	P	S	Si	Cr	Ni	Mo	N	Fe
0.03	2	0.045	0.03	0.75	16.00-18.00	10.00-14.00	2.00 – 3.00	0.1	BAL

3.2 SAMPLE PREPARATION

3.2.1 2-D Linear Plane-Strain Machining

A custom-built linear machining device, which ensures plane-strain (2-D) conditions, was used to deform the surface substrate from commercially available 316L stainless steel plates, which was sectioned into 60 mm x 45 mm x 3mm samples, using high strength steel (HSS) tools with a rake angles of +20° and 0°, with a constant cutting depth of a_o=150 µm and a constant tool velocity of 12.5 cm/s. The deformation processes were carried out at room temperature.

3.2.2 Vickers Hardness

Substrate samples for indentation hardness measurements using the Vickers micro-hardness test were prepared by metallographic methods of mechanical grinding and polishing on the cross-sectional side following 2-D linear plane-strain machining.

3.2.3 Vibrating Sample Magnetometer

Samples for magnetometry have been prepared from the as-received state and after the 2-D linear plane-strain machining by metallographic methods of mechanical grinding and polishing from the substrate side, i.e., the non-machined surface, until about 100 microns thick sections were obtained.

3.2.4 Scanning Electron Microscope

Samples for SEM investigations have been prepared by metallographic methods, e.g. grinding and polishing, in cross-sectional geometry following 2-D linear plane-strain machining.

3.2.5 Transmission Electron Microscope

TEM samples of the substrate surface were prepared by thinning sections to about ~ 75 µm thickness from the bulk side, leaving the surface-side unpolished. Discs of 3 mm diameter have been punched out from the ~75µm thick sections, followed by electro-polishing with a Fischione Model 140 twin-jet electro-polisher using an electrolyte solution of 73% ethanol, 10% butyl cellosolve, 8% perchloric acid, and 9% water at 298 K and 35 V, in order to obtain electron transparent thin sections from the plastic deformation modified substrate surfaces. The TEM discs were electro-polished from the bulk-substrate side only to ensure the surface substrate would be probed when investigated in the TEM.

3.3 EXPERIMENTAL SETUPS

3.3.1 X-Ray Diffraction

A Bruker D8 Discover x-ray diffractometer has been operated at 40 V and 40 A with Copper K-alpha radiation ($\lambda = 0.15406$ nm) using a LynxEye detector in a symmetric Bragg-Brentano setup to obtain X-ray diffraction patterns from the 316L material. A XRD scan was performed with a step size of 0.02° with a scan speed of 1 second per step and a range from 40° to 85°. This ensured that the major diffraction maxima associated with the expected and the possible major matrix phases in the 316L, e.g. austenite, ferrite and martensite, would be probed.

3.3.2 Vibrating Sample Magnetometer

A Lakeshore vibrating sample magnetometer (VSM) model 7404 with a maximum magnetic field of 21.7 kOe (2.17 T) at 298 K has been used for magnetometric measurements. The maximum externally applied magnetic field strength used in the experiments was 20 kOe (H_{max}). The scan of the hysteresis magnetization loop was performed (0 kOe to $+H_{max}$ to $-H_{min}$ to H_{max}) for obtaining the saturation magnetization at a scan rate of 157.233 Oe/s and a step size of 0.629 kOe.

3.3.3 Vickers Hardness

Microhardness was measured with a Leco M-400-G Vickers hardness testing machine using a load of 50g and a dwell time of 10s. The cross-sectional side of the substrate surface is

sampled as close to the machined surface as possible without experiencing surface effects on the indent. The central regions of the indents are located as close to the plane-strain machined substrate surface as ~10 μm..

3.3.4 Scanning Electron Microscope

For the SEM imaging in secondary electron (SE) mode and/or in back-scatter electron (BSE) mode, a Phillips XL-30 field emission instrument operated at 20 kV has been used. For orientation imaging microscopy (OIM) electron back-scatter diffraction (EBSD) patterns have been collected with a spot size of 5 and a step size of 200 nm in a forward scattering geometry set-up with tilting the sample surface by 70° towards the scanned electron beam. EBSD data sets have analyzed using the TSL OIM Analysis software package.

3.3.5 Transmission Electron Microscope

The microstructure of the substrate surface was characterized by imaging and diffraction based analyses methods of TEM using a JEOL CM200X instrument with a tungsten filament and a JEOL JEM-2100F field emission TEM instrument. Both instruments have been operated at 200 kV.

Grain size determination is performed through the use of several DF micrographs. The FCC {111} diffraction was selected, and the aperture is placed over one of the g-vectors. The DF micrograph is collected, and the aperture is moved to a difference g-vector, and this process is repeated until the complete set of g-vectors that comprise the FCC {111} diffraction ring for a

given field of view is recorded. The micrographs are combined to identify as many grains as possible, and are measured to determine the grain size and grain size distribution for the sample condition.

A novel TEM technique for acquisition of data sets for characterization of nano and ultrafine grain sized materials can be accomplished through the use of electron beam precession with spot diffraction pattern recognition is called precession electron diffraction (PED). Electron diffraction spot patterns are collected through an external CCD camera attached to the TEM viewing screen while the area of interest is scanned by an incident quasiparallel nano-beam (<2 mrad). The electron beam is precessed around the optical axis of the microscope for reduction of dynamical effects, which acquires easier to index electron spot diffractions [81]. In PED, the precessed electron beam creates a cone where the pivot point is focused on the sample, which produces a hollow-circle array of diffraction spots at the exit plane of the sample. Once a counter-precession signal is applied and adjusted to the level of the back focal plane of the objective lens, a pseudostatic diffraction image is observed. A dedicated external hardware unit generates the beam scanning and precession diffraction simultaneously to control the beam pivot point through the pre-selected scan area [82]. The advantage of using a precessed beam for collecting diffraction spot patterns is that it has been shown to increase the number of reflections observed that exhibit a quasi-kinematical integrated intensity causing higher order Laue zone reflections to be excited [83]. This technique allows the ability to acquire reliable orientation/phase maps with a spatial resolution down to 2 nm on a TEM with a field emission gun [84]. Once the PED spot patterns for the area of interested has been collected, phase and orientation identification for each spot pattern is performed through comparison with previously generated templates, which are kinematical electron diffraction patterns calculated based on the expected crystallographic phases

expected in the scanned area. This TEM technique will be able to extract a variety of information on the microstructure such as grain size of all the different phase constituents, internal strain, grain boundary character distributions, texture, and phase distributions throughout the material [85]. For the deformed 316L austenitic stainless steel samples, the precession angle was set to 0.7° with a step size of 5 nm.

3.3.6 Heat Treatments

The heat treatments were performed using ULVAC MILA-3000 mini-lamp annealing system, which provides capability for controlled atmosphere, either high-vacuum or inert-gas backfilled conditions, thereby reducing effects from surface oxidation during heat treatments. The melting point of 316L is 1399°C (~1672 K), which indicates that the recrystallization temperature is in the range of 284°C to 562.85°C. In an effort to determine the recrystallization temperature, heat treatment experiments of 350°C to 650°C with intervals of 50°C were performed. The samples were brought up from room temperature to the heat treatment temperature using a ramp time of one minute and held at the heat treatment temperature followed air-cooling to room temperature. Beside the recrystallization determination experiments, high and low temperature experiments were conducted. The high temperature experiments were conducted at 800°C for 5 minutes, which were heated up with a ramp time of one minute followed by air-cooling to room temperature, to understand martensite reversion and grain boundary structure change. The low temperature experiments were conducted at 350°C for 500 hours, which were heated up with a ramp time of one minute followed by air-cooling to room temperature, to understand martensite reversion, recovery related strain relief, and grain stability.

4.0 RESULTS AND DISCUSSION

4.1 AS DEFORMED CHARACTERIZATION

As discussed in the background chapter, the average shear strain (γ) and strain rate ($\dot{\gamma}$) in the chip can be estimated using equations (9) and (10) [61, 62] based on the actual permanent shape changes realized in the chips as measured by a precision 0-6 inch micrometer. Figure 3 shows the measured γ and the $\dot{\gamma}$ for a range of tool velocities. The γ imparted to the chip was found to be quite insensitive to the tool velocity, remaining relatively constant with values ranging from 2.22 to 2.07 for the tested tool velocities. However, the $\dot{\gamma}$ increases rapidly ranging from ~$1.7 \times 10^2 s^{-1}$ to ~$1.7 \times 10^3 s^{-1}$ as a function of tool velocity in the range of $2.5 cms^{-1}$ to $25 cms^{-1}$. The measured strain values are comparable to other SPD techniques, such as ECAP, HPT, and SMAT, which have confined geometries or cannot be performed in a single pass at room temperature. Additionally, the strain rate is significantly higher as compared to conventional cold deformation processes or SPD techniques [86, 87].

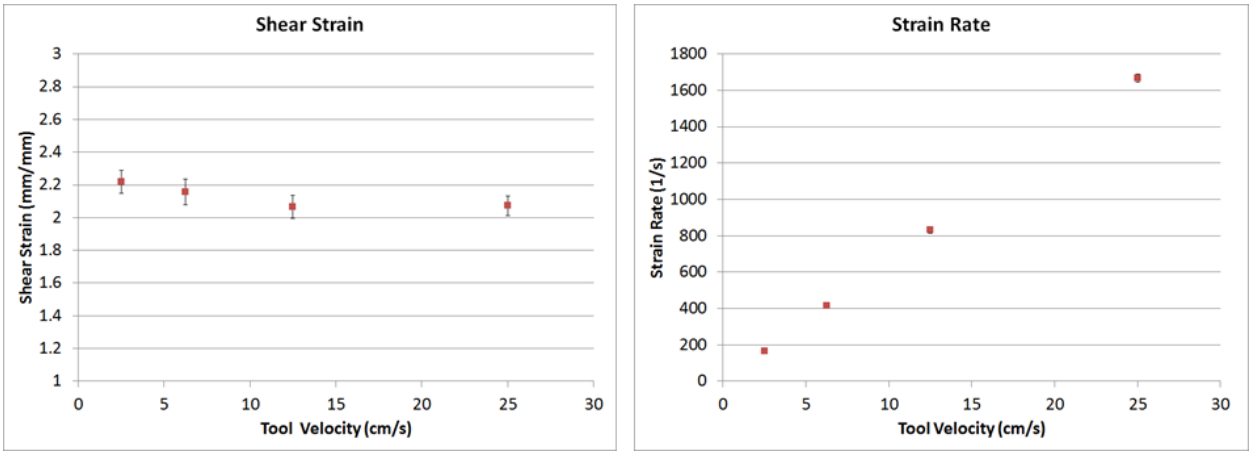

Figure 3 ïShear strain and strain rates for the 4 tool velocities of the 316L chips

The fractions of SIM induced by the plastic deformation processing have been measured by XRD and VSM (Figure 4). The measured fractions of SIM indicate little dependence on the strain rate or tool velocity for tool velocity above 2.5 cm s^{-1}. There is an increase from the as-received state of ~0.6% to ~9% for 2.5 cm/s and ~3% for all velocities above 2.5 cm/s (Figure 4). These values are extremely low volume fraction of SIM produced when compared to conventional cold rolling to comparable strains [86] in 316L. Based on the shear strain produced from the linear plane-strain machining, ~82-87% thickness reduction in conventional cold rolling at room temperature would be required to produce similar shear strain magnitudes, in which ~50% SIM would be expected [88]. However, the strain rates are much higher than in conventional cold rolling, which could explain the minimal SIM produced. Adiabatic heating occurs as result of high strain rates, thus presumably suppressing SIM formation [89, 90].

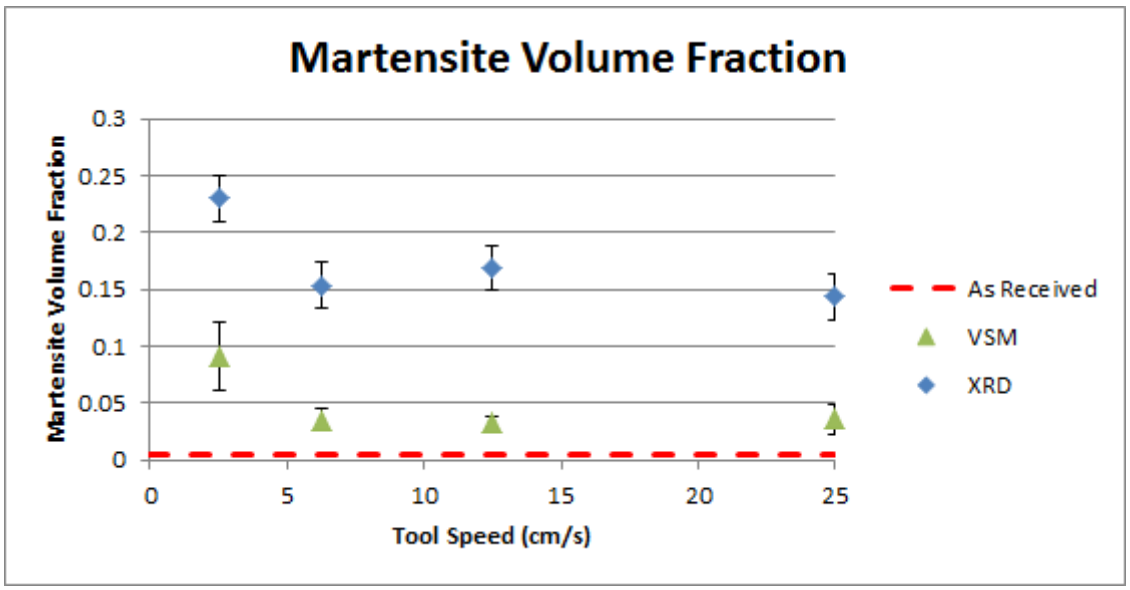

Figure 4 ïMartensite volume fraction of the 316L chip as determined by XRD and VSM

While the trends in the effects of strain rate or tool velocity are similar in the SIM fraction measurements obtained by XRD and VSM, quantitative differences are clearly noticeable Figure 4). The XRD measurements consistently delivered significantly larger magnitudes for the SIM than the VSM measurements (Figure 4). X-ray diffraction (XRD) is considered a bulk surface characterization technique due to the large areas sampled, which provides representative data sets of the polycrystalline material. However, the disadvantage is the shallow penetration depth of the x-rays used in a typical laboratory instrument used for XRD with Cu-Ka radiation, for instance. The x-ray penetration depth through the material can be determined by using equation (13) [91]:

$$I = I_o e^{-2\mu x} \quad (13)$$

Where μ is the weighted mass absorption coefficient of the material [91] and x is the thickness of the material. To determine the penetration depth, the intensity is assumed to be

that $I = \frac{1}{1000} I_o$, which is the beam intensity at which it is considered negligible. The calculation shows the penetration depth of the x-rays into the 316L is at maximum ~16 µm. Figure 5 compares XRD scans of the chips processed at 0° tool angle with a tool velocity of 2.5 cm/s, 6.25 cm/s, 12.5 cm/s, and 25 cm/s with the as received 316L. For each of the scans with the normalized intensity $I(2\theta)/I_{max}$ is shown, where I_{max} is the maximum intensity measured for the strongest peak, which is shown to be the {111} FCC austenite phase peak. The {111} austenite peak intensity has been determined after deconvolving the {110} BCC martensite peak for proper quantitative analysis. The as received material shows the typical peak positions and intensities of undeformed 316L with a relatively low intensity {110} peak of BCC martensite phase. In attempts of quantitative XRD analysis, only the {111} FCC peak was considered since all other FCC phase peaks were significantly reduced in intensity upon deformation processing. Analysis of the XRD line profiles reveal no significant changes in the peak positions or uniform strain after deformation processing, which may indicate little residual stress is induced from the deformation process; however, there is considerable peak broadening in all FCC and BCC peaks, which can be attributed to stored non-uniform strain and grain size reduction [91]. The full width at half maximum (FWHM) or the peak broadening, b, is a metric that allows for analysis of the stored non-uniform strain and determination of associated elastic stress magnitudes using equations (14) and (15), where E is [91] Young's modulus

$$b = -2\varepsilon \tan\theta \qquad (14)$$

$$\sigma = E\epsilon \qquad (15)$$

The peak broadening analysis shows significant broadening for the {111} austenite peaks of 0.314°, 0.356°, 0.297°, and 0.313° for the chips produced with a tool velocity of 2.5 cm/s, 6.25 cm/s, 12.5 cm/s, and 25 cm/s respectively. These peak broadening value are determined by measuring the actual peak broadening and removing the instrumental peak broadening of the {111} austenite peaks. The actual peak broadening was measured to be 0.469°, 0.511°, 0.452°,and 0.468° for the chips produced with a tool velocity of 2.5 cm/s, 6.25 cm/s, 12.5 cm/s, and 25 cm/s respectively along with an instrumental peak broadening of 0.155° Assuming the measured peak broadening observed for all conditions is associated entirely with non-uniform strain stored in the deformation processed microstructures according to equation (12) provides a strain magnitude and associated elastic stress magnitude according to equation (13), which is documented in Table 2. The strain and stress magnitudes indicate a significant amount of stored non-uniform strain, but there is not a significant difference between the different tool velocity conditions. The grain size can be determined from peak broadening in powder type XRD data through the use of equation (16) [92], where K is a dimensionless shape factor, 0.94 is used, β is the peak broadening at FWHM, and τ is the grain size.

$$\tau = \frac{K\lambda}{\beta \cos\theta} \qquad (16)$$

In the case where only grain size effects are considered to account for the x-ray peak broadening, the grain size for all tool velocity conditions are calculated from equation (16). Results from this grain size analysis of the observed peak broadening are shown in Table 2. The tool velocity did not result in significant differences in grain size as determined by XRD. The magnitudes of the grain size, uniform and non-uniform stress and strain, and peak broadening determined here for the plane strain machining deformed 316L material are similar to reports for

316L [86] and interstitial-free steel after SPD by ECAP. The different tool velocity conditions show a change in the relative intensities of the I_{111}/I_{200} and I_{111}/I_{220} peaks and an increase in the intensity of the I_{110} peak of the BCC martensite. Such changes are consistent with a change in texture and a potential increase in the amount of SIM, the martensite volume fraction (MVF), induced by the machining process.

Table 2 ïQ u a n t i t a t i v e r e s u l t s o f 3 1 6 L c h i p s a t t h e 4 d i f f e r

Velocity (cm/s)	Microstrain	Stress (GPa)	Grain Size (nm) - XRD	Hardness (VHN)	Tensile Strength (MPa)	GS Strength Contri-bution (%)
As Received	-	-	~20000	159	~ 515	11
2.5	0.007 +/- 0.001	1.323 +/- 0.200	~30	524 +/- 18	~ 1800	80
6.25	0.008 +/- 0.001	1.504 +/- 0.200	~25	517 +/- 29	~ 1760	90
12.5	0.007 +/- 0.001	1.252 +/- 0.200	~30	498 +/- 10	~ 1690	85
25	0.007 +/- 0.001	1.323 +/- 0.200	~30	501 +/- 12	~ 1690	85

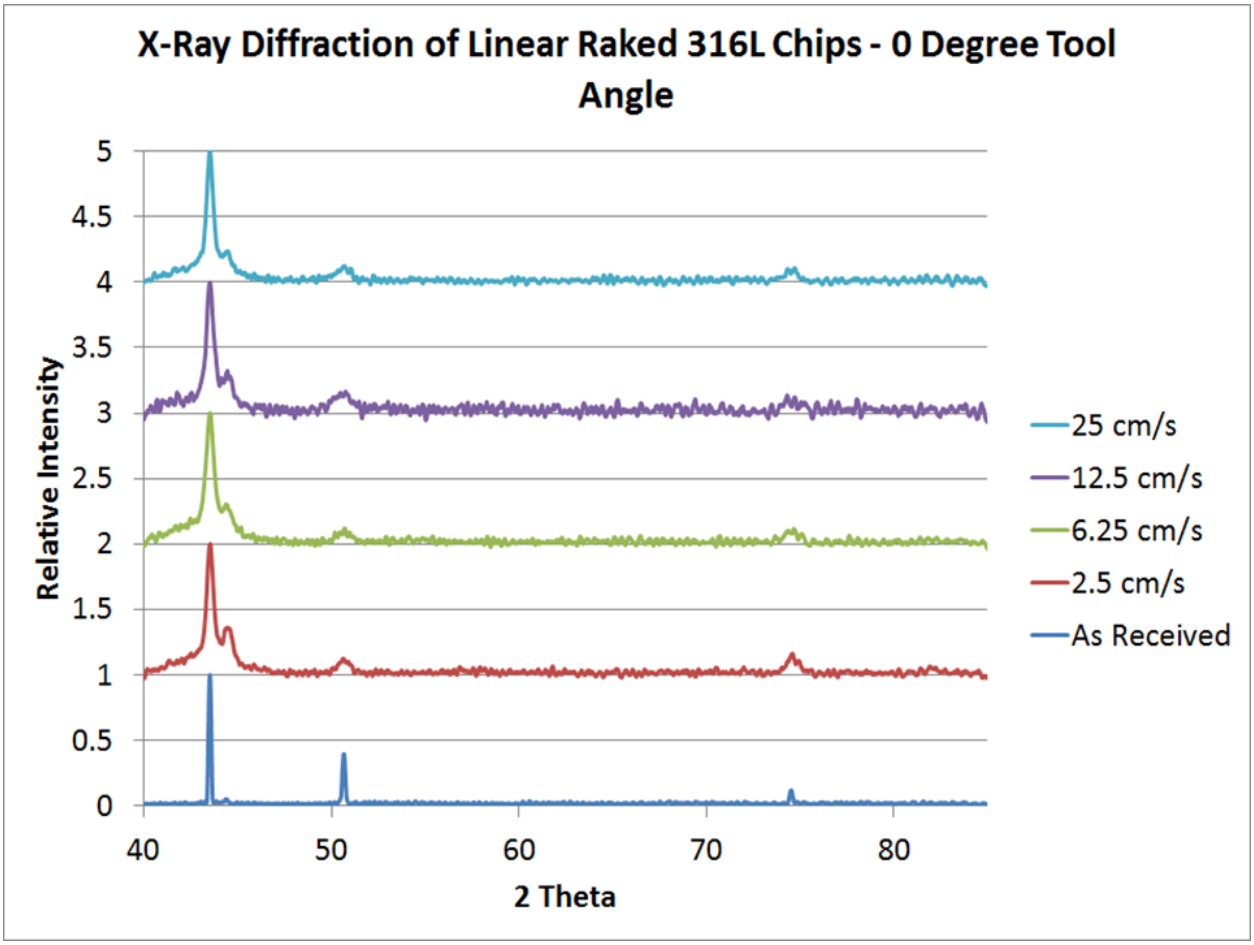

Figure 5 iXRD line scan of 4 different tool velocities for the 316L chips

A quantitative estimation of phase fractions can be used to determine the martensite volume fraction (MVF) due to formation of strain induced martensite (SIM) in the 316L material based on the principle that the total integrated intensity of all diffraction peaks for each phase in a mixture is proportional to the volume fraction of that phase [91]. The integrated intensity has two attributing principle factors: The instrument factor and the material scattering factor, R_{hkl}. The instrument factor is based on the XRD beam geometry characteristics such as cross-sectional area of incident beam, wavelength of incident beam, and radius of diffractometer circle; thus, it is a constant for all phases and will be canceled out when comparing ratios of intensities for the two phases. The material scattering factor, on the other hand, will be different for the two phases, and is based on the multiplicity factor, lattice parameter, Lorentz-Polarization factor, temperature factor, absorption factor, and structure factor, as seen in equation (17). Cullity [91] shows the relationship between the measured intensities of the austenite (γ) and martensite (α), the material scattering factors of the two phases, and the volume fraction of each phase (C_γ and C_α) in equation (18). One of the drawbacks from the use of a Copper XRD source in the experimentation conducted here is the limited number of BCC peaks that can be observed. Therefore, for the quantitative estimation of phase fractions only the first FCC and BCC peaks will be used. The values for the factors contributing to the material scattering are tabulated in Table 3. The values for Debye-Waller factor, B(T), of the temperature factor are derived from experimentally determined elemental phonon density of states with an accuracy between 2-3% [93]. The FCC and BCC peaks are very close in proximity to each other. So, a curve fitting and peak analysis software, Fityk, was used for deconvolving the FCC and BCC peaks for quantitative analysis [94]. According to the XRD MVF calculations, the as received material has a MVF of 1.78%.

The XRD MVF follows the same trend as the data collected through the VSM, but with at higher values as shown in Figure 4. The 2.5 cm/s tool velocity has a MVF of ~23%, while all other velocities produced a MVF of ~15%. The differences in the MVF between XRD and VSM measurements may be explained by two possible scenarios. The XRD measurements are analyzing only the surface of sampled area of the chips; meanwhile, the VSM is a bulk MVF measurement tool. The increase in MVF from the XRD calculations may indicate a gradient of strain-induced martensite (SIM) with the measured surface having a higher concentration. Another possible explanation is related to the effects from texture resulting from the deformation process. If the sample were to have a texture, it could possibly give a misleading MVF value. Further analysis will be necessary to investigate the possible texture effects, which is undertaken in the TEM analysis of the chips.

$$R_{hkl} = \left(\frac{1}{v^2}\right)\left[|F|^2\rho\left(1+\frac{cos^2 2\theta}{sin^2\theta cos\theta}\right)\right](e^{-2M}) \quad (17)$$

$$\frac{I_\gamma}{I_\alpha} = \frac{R_\gamma C_\gamma}{R_\alpha C_\alpha} \text{ Ą } C_\alpha = \frac{1}{\left[\frac{I_\gamma R_\alpha}{I_\alpha R_\gamma}+1\right]} \quad (18)$$

Table 3 ïParameters of the material scattering factor for XRD MVF determination

	FCC (111)	BCC (110)
Multiplicity Factor [91]	**8**	**12**
Lattice Parameter [91]	**3.515 Å**	**2.78 Å**
Lorentz-Polarization Factor (based on θ)	$1+\frac{cos^2 2\theta}{sin^2\theta cos\theta}$	$1+\frac{cos^2 2\theta}{sin^2\theta cos\theta}$
Temperature Factor (based on B(T) and θ) **[93]**	$B(T) = 0.5577$ Å^2 $M = B(T)s^2$ $s = \frac{\sin\theta}{\lambda}$	$B(T) = 0.3250$ Å^2 $M = B(T)s^2$ $s = \frac{\sin\theta}{\lambda}$
Absorption Factor	**Neglected due to independent of θ**	**Neglected due to independent of θ**
Structure Factor (based on θ and constants for atomic form factor from [95])	$F_{hkl} = 4f$ $f(q) = \sum_{i=1}^{4} a_i e^{-b_i q^2} + 4c$ $q = \frac{\sin\theta}{\lambda}$	$F_{hkl} = 2f$ $f(q) = \sum_{i=1}^{4} a_i e^{-b_i q^2} + 4c$ $q = \frac{\sin\theta}{\lambda}$

The as received material exhibits a Vickers microhardness of 159 VHN (corresponding to 515MPa tensile strength). After 2-D plane strain machining with the 0° tool angle at the different tool velocities, the michrohardness increased significantly as tabulated in Table 2, with maximum values of about 500-520 VHN (~1690 ï~1800 MPa tensile strength).

Using a Hall-Petch type relationship between mechanical strength and the average grain size of the polycrystalline aggregates of 316L, as expressed for instance in equation (19), a grain size corresponding to the measured strength values can be estimated.

$$\sigma_o = \sigma_i + kD^{-\frac{1}{2}} \qquad (19)$$

In equation (19) σ_o is the yield stress, σ_i is the ñfriction stressò resistance of the crystal lattice to dislocation movement, k is the strengthening coefficient, which measures the relative hardening contribution of the grain boundaries, and D is the average grain diameter. The strengthening coefficient for 316L is determined to be ~0.25 MPa $m^{1/2}$ [89, 96] . Relationships of the Hall-Petch type akin to that for the yield stress shown in equation (19) have also been shown to be valid for changes in hardness of polycrystalline ductile metals and alloys. Hence, using average grain sizes of the 316L determined by XRD, SEM, and TEM measurements it is possible to evaluate the grain size strengthening contributions that would be expected based on the Hall-Petch type behavior. The significant reduction in grain size observed is actually the grain size equivalent. Because the heavily deformed material has not been annealed, the material has not been able to recrystallized and develop the different orientations to positively identify the refined grains. The determined grain size equivalent from the deformation process will be referred to as the ñgrain sizeò from

The grain size strengthening contribution to the tensile strength is thus calculated as ~1700 - ~1800 MPa for the various tool velocities, which would account ~80% - ~90% of the total tensile strength measured by the microhardness test based on the estimated grain size as de-

termined by XRD. The remaining ~10 - ~20% of the total tensile strength can presumable be attributed to other strengthening mechanisms, including contributions from stored strain, martensite phase fraction, and texture. To more accurately identify the extent of the contributions from stored strain, strained induced martensite phase fraction, and texture, conventional and advanced TEM analysis will be required.

Analysis of the 2-D linear orthogonal machined chips has shown very similar properties after processing with the tool velocities of 6.25 cm/s, 12.5 cm/s, and 25 cm/s with the exception of strain rate; meanwhile, the 2.5 cm/s condition has shown to have a similar properties to the other higher velocity conditions with the exception of strain rate and volume fraction of martensite formed. Even though the MVF is higher in the 2.5 cm/s, the sample has relatively similar hardness values as compared to the velocities might be explained by the fact that the grains might be larger and could offset the increase is MVF ï the effect of the grain size has been shown to possibly have a strong effect on hardness, which will be further investigated when the stored strain is analyzed in the TEM. One possible explanation for the difference in MVF in the 2.5 cm/s tool velocity condition from the other velocities that will also take into account the differences in strain rate is the effect temperature during the machining process.

The measured maximum temperature rise was determined by infrared-thermography was performed with an infrared camera, FLIR systems Inc., model FLIR A325sc for the surface temperature field measurements captured at 60 frames per second. Using the estimated strain and strain rate data shown in Figure 3[79], the temperature rise in the chip can be estimated theoretically by coupling the work of plastic deformation to the temperature at the shear plane [97].

$$\rho C_p dT = (1-\beta)\, \sigma(\varepsilon,\dot{\varepsilon},T)\, d\varepsilon \qquad (20)$$

Equation (20) states that an increment in plastic strain, $d\varepsilon$, equates to an equivalent increment in temperature, dT. Here ρC_p is the heat capacity of 316L and $\sigma(\varepsilon, \dot{\varepsilon}, T)$, is the Johnson-Cook model for describing flow stress as a function of strain, ε, strain rate, $\dot{\varepsilon}$, and temperature, T [98]. The calculated flow stress is then multiplied by the pre-factor (1-β), where β describes the fraction of the heat transported away from the chip by the bulk material [99]. The factor β is given by:

$$\beta = \frac{1}{4\alpha} erf\sqrt{\alpha} + (1+\alpha) erfc\sqrt{\alpha} - \frac{e^{-\alpha}}{\sqrt{\pi}}\left(\frac{1}{2\sqrt{\alpha}} + \sqrt{\alpha}\right) \quad (21)$$

Where α is a function of plane-strain machining parameters V_c and a_0, the shear angle φ, and thermal diffusivity of the bulk material κ [97]:

$$\alpha = \frac{V_c\, a_0 \tan\varphi}{4\kappa} \quad (22)$$

By rearranging the expressions in equations (20-22) the total temperature rise is determined by the integral [100]:

$$\int_{T_0}^{T_{calc}} \frac{\rho C_p(T)}{1-\left(\frac{T-T_r}{T_m-T_r}\right)^m} dT = (1-\beta)\left(A\varepsilon + \frac{B}{n+1}\varepsilon^{n+1}\right)\left(1 + C\, ln\left(\frac{\dot{\varepsilon}}{\dot{\varepsilon}_0}\right)\right) \quad (23)$$

In equation (23), A, B, C, $\dot{\varepsilon}_0$, *m* and *n* are material constants have been determined through a combination of analytical and empirical techniques by Chandrasekaran *et al.* [101], and T_m and T_r are the material melting temperature and room temperature, respectively [98].

The temperatures calculated using equation (23) are similar, but slightly higher than the temperature rise magnitudes measured by IR-thermography as shown in Table 4. The temperature differences can be accounted for due to the fact that the Johnson-Cook model uses an idealized case where all mechanical work applied to the chip during deformation transforms to heat, but does not account heat transfer away from the chip such as conduction or convection. The measured temperature rise is shown to be significantly lower in the 2.5 cm/s as compared to the other velocity conditions. Hence, this difference in the mechanical work related heating of the chip material appears suitable to explain the differences in MVF measured through XRD and VSM. The amount of SIM formed per unit of strain is expected to increase with a reduction in temperature for all temperatures below which SIM can be formed, which is agrees with the measured temperature rise values from IR-thermography. Additionally, the IR-thermography shows a temperature profile across the cross section of the chip. Temperatures from adiabatic process heating are higher in the regions central to the volume of chip than for the surfaces of the chip. The SIM fractions are highest near the surfaces where temperatures reach lower maximum values and cooling is more rapid establishing conditions for reversion of SIM for much shorter periods of time as compared for the center of the chip; therefore, a gradient is expected to develop from the central region to the surface region of chip. Another possible explanation for the SIM gradient is the mechanical stabilization of the austenite. Martensitic transformation typically occurs without diffusion with paraequilibrum, a condition where substitution atoms do not partition the atoms between phases during the transitions creating a minimal free energy condition [102]. In theory, all of the austenite should transform into martensite; however, it is observed that this is not the case [103]. The interface between martensite and austenite grains has been shown to contain glissile dislocations whose motion could be slowed down by the defects

in the austenite; therefore with a larger enough strain, the introduction of a larger number of defects in the austenite will completely prevent movement of the interfaces and stopping the martensite transformation process [104, 105]. Even though mechanical stabilization of the austenite is possible, it is unlikely the primary mechanism being observed in the 316L 2-D linear plane-strain machined chips. Characterization has shown strain to be relatively uniform in the chip; therefore, a SIM gradient would not be expected, which is not observed indicating the adiabatic temperature most likely is the cause of the SIM gradient.

Table 4 ïExperimental and calculated temperatures based on the deformation process [79]

Velocity (cm/s)	Calculated Temperature (°C)	Measured Temperature (°C)
As Received	-	-
2.5	106	77.9
6.25	152	-
12.5	193	125.4
25	253	197.3

Figure 6 A-H show bright field (BF) micrographs and associated selected area diffraction patterns (SADP) of the chips deformed with a 0° tool angle at the various tool velocities, respectively. All tool velocities except the 2.5 cm/s tool velocity show morphologically very similar microstructures with large defect content and significant grain refinement, including very similar SADPs. The SADPs reveals a moderate radial spread and a significant orientation spread, which would be consistent with moderate levels of non-uniform stored strain and significant grain refinement. The deformation caused by the 2.5 cm/s tool velocity creates a microstructure with large defect content with grain refinement, but the grains are noticeably larger than observed in the other tool velocity conditions. The SADP pattern for the 2.5 cm/s tool velocity condition reveals a larger radial and smaller significant orientation as compared to the other tool velocity

conditions, which indicates more stored strain and larger grain size. One problem that arises when analyzing the SADP is spacing between the FCC {111} and BCC {110} spots are very close and overlap, which makes the analysis of stored strain and strain induced martensite difficult. To overcome this issue, a more quantitative analysis of the TEM SADP can be conducted using the profile analysis of the selected area diffraction (PASAD).

Figure 7 shows a PASAD for all the velocity conditions of the chips. The PASAD method transforms the two-dimensional ring-like SADP data into an electron diffraction intensity profile by azimuthal integration and applying the pseudo-Voigt function for determining peak shape related parameters [106]. The PASAD data are a plot of the integrated diffracted intensity versus the magnitude of the diffraction or scattering angle, and can be interpreted somewhat similar to a XRD powder diffractometer trace or scan. The PASAD indicates for the 6.25 cm/s, 12.5 cm/s, and 25 cm/s velocities that there is very little strain induced martensite, and the majority of the radial spread is related to stored strain. The amount of stored strain is still minimal as compared to other tool angles previously studied on 316L stainless steel [37]. Because all three velocity conditions exhibit similar peak intensities for the strain induced martensite that also supports the VSM work of similar MVF and the radial spread becomes wider as the tool velocity is increased, the stored strain can be assumed to be directly related to the strain rate. The increasing stored strain can be confirmed with a precession electron diffraction orientation imaging microscopy study of the deformed material. On the other hand, the 2.5 cm/s exhibits noticeable peaks in PASAD resulting from the strain induced martensite, which is obvious when observing the BCC {211} peak. This is in line with previous VSM results showing a significant increase in the 2.5 cm/s velocity chip as compared to the other velocities. The 2.5 cm/s chip is similar to the other

chips with an observable radial spread induced from stored strain; however, the low tool velocity chip differs with discernible increase in the strain induced martensite.

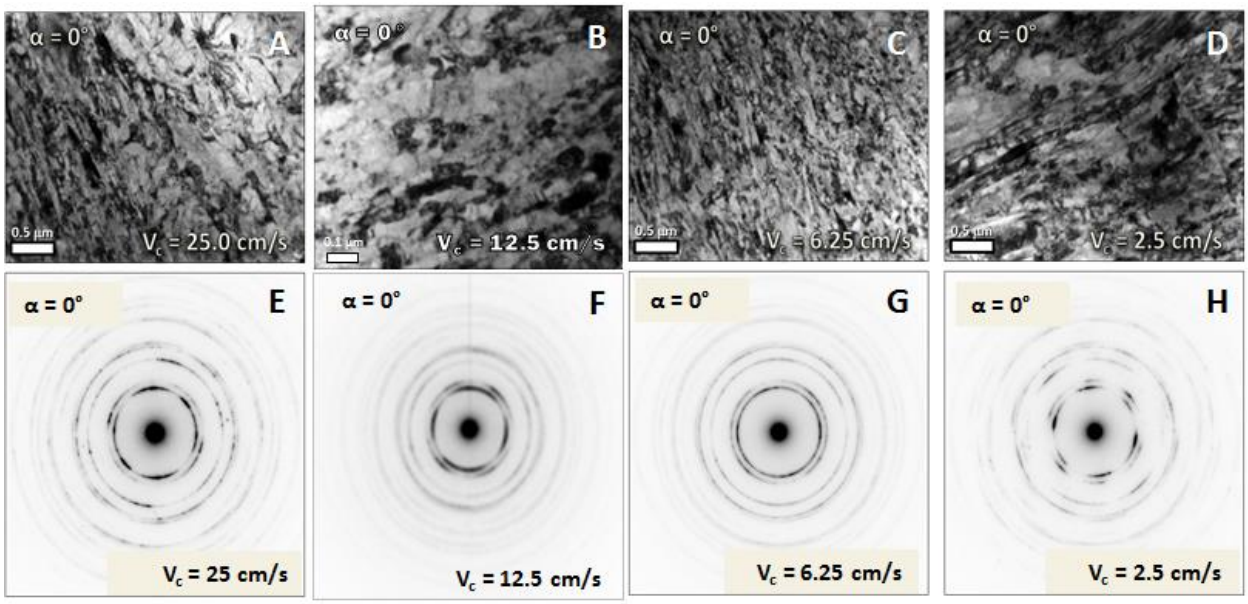

Figure 6 ï TEM BF micrographs with the associated SADPs for the 4 different tool velocities for the 316L chips

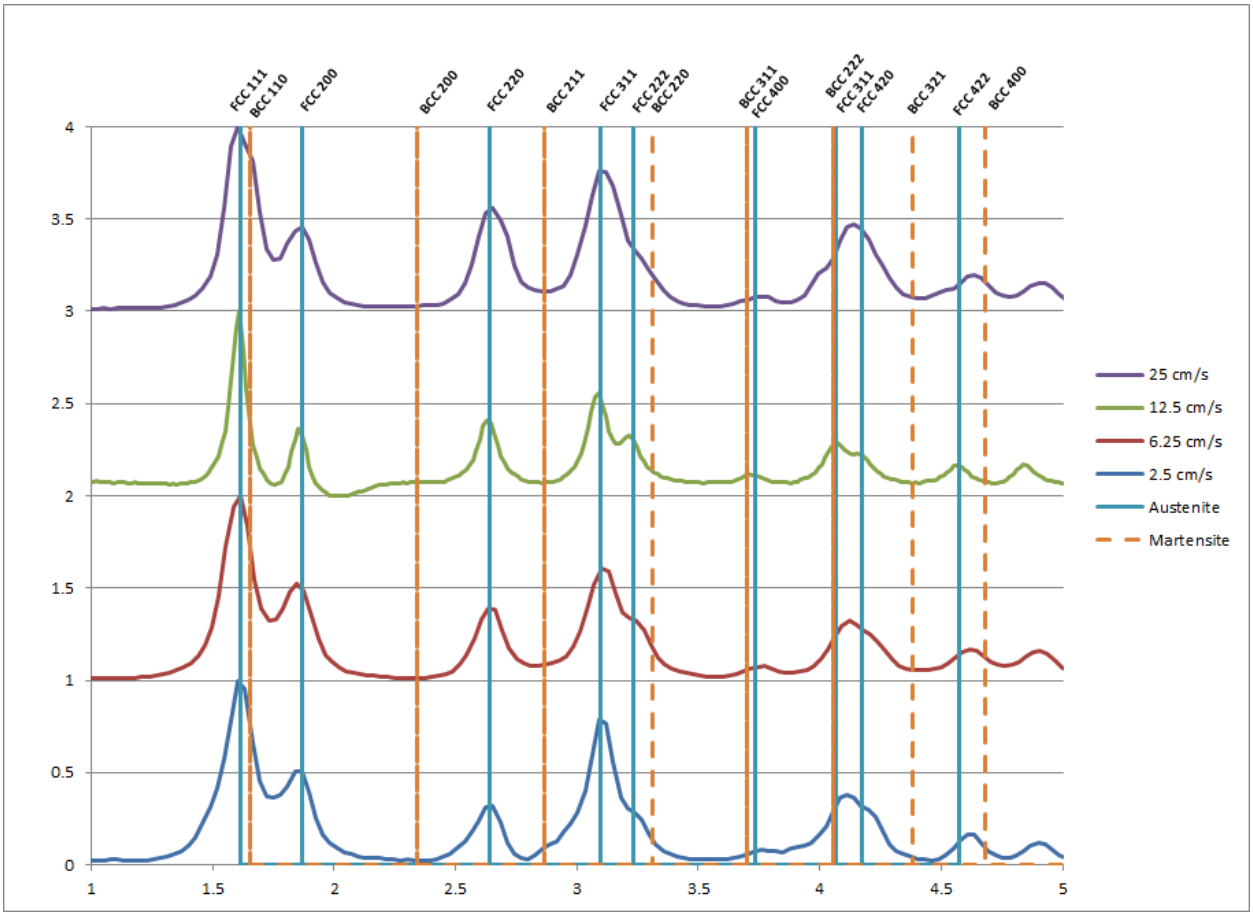

Figure 7 ïPASAD data plot for the 4 different tool velocities of the 316L chips

Table 5 ïTEM DF grain size analysis for the 4 different tool velocities of the 316L chips

Velocity (cm/s)	Grain Size ïDark Field (nm)
As Received	~20000
2.5	73 +/- 23
6.25	45 +/- 7
12.5	43 +/- 5
25	50 +/- 3

An analysis of the dark field (DF) micrographs was performed to determine the average grain size and grain size distribution. DF micrographs for all the different g-vectors that comprise the FCC {111} diffraction ring for a given field of view. These micrographs were combined and used to determine the grain size and grain size distribution. The grain size is tabulated in Table 5, and shows significant grain refinement from the as-received material. The 6.25, 12.5, and 25 cm/s show similar grain size; meanwhile, the 2.5 cm/s shows a significantly larger grain size relative to the other tool velocities. The differences in the strain rate may be able to explain the differences in the measured grain sizes. It might be possible that above a certain strain rate value, which occurs between the strain rates observed in the 6.25 cm/s and 2.5 cm/s, that geometric dynamic recrystallization of the microstructure is observed. Before this phenomenon can be ascertained, further information regarding grain shape, texture, stored strain, and grain boundary character distribution is necessary, in which PED-OIM can be used as the tool to collect this information.

PED-OIM analysis was performed on specimens obtained for the 25 cm/s and 12.5 cm/s tool velocity conditions of the 0° chip. Figure 9 shows the inverse pole figures for the two chip conditions. Both conditions show grains with an irregular shape and grain boundaries exhibiting roughness as a result of the 2-D linear plane strain machining. The definition of irregular shape used here relates to the grains having no defined shape with any defined lines of symmetry, which can be expected for a deformation that involves shearing.

It seems as the velocity is increased, the grains within the material tend to shift from a high probability of irregular shaped grains to a high probability of elongated grains. This may be a direct result of the associated increase in the deformation related elevation in temperature of the chip material and the strain rate. The stored strain of the grain interiors can be assessed by the point-to-point disorientation. As shown in Figure 9, the point-to-point disorientations of the grains are affected by the tool velocity increase from 12.5 cm/s to 25 cm/s. The point-to-point disorientation graphs are representative of the grains for the associated condition. For the 25 cm/s machining condition the disorientation metrics reveal a high amount of intragranular strain with a developed dislocation structure sub-cell network. The grains typically exhibit several intragranular point-to-point disorientations exceeding 10 ę Meanwhile, for the plastic deformation processing with the lower tool velocity of 12.5 cm/s intragranular point-to-point disorientations remain small with typically 1- 2 ę and very 5 ę Notably, the accuracy of the orientation indexing of the TEM PED-OIM orientations is limited to the default setting of the ASTAR software. The disorientation metric reveals the significant differences for the intragranular volumes regarding internal strain storage as a direct result of the increase in velocity. As the material is deformed, defects are induced in the material usually in the form of dislocations. These defects form a network of dislocation that become HAGBs, which becomes a non-equilibrium structures with excess free energy stored in the grain boundaries. It can be stated that the recovery and recrystallization processes are dynamic during the SPD related grain refinement leading to new stress free interiors with all the defects stored in the grain boundaries. Because the process is indeed dynamic, the new formed refined stress free grains are exposed to plastic straining introducing internal strain, which is shown that the higher strain rates deposit a

larger point-to-point disorientation during the deformation process. This is consistent with results shown in the SADP where more radial peak broadening is observed in the higher tool velocity condition meanwhile the SIM is measured to be the same using VSM for the two conditions.

Figure 8 shows the pole figures for the 12.5 cm/s and 25 cm/s displaying elements of the texture established in the plan-view orientation of the chips as determined by TEM based PED-OIM. The weak texture present in the 12.5 cm/s tool velocity processed microstructure increases in strength towards a more noticeable {100}-type cube texture component developing as the strain rate is increased. For the respective grain boundary networks, the strong link fractions are significantly reduced from ~0.350 in the as received material to 0.08 +/- 0.02 and 0.06 +/- 0.01 for the 12.5 cm/s and 25 cm/s tool velocity conditions respectively. Even though there is significant grain refinement ïmeasured to be ~40 nm through PED-OIM for both chip conditions, very few low energy grain boundaries exists in the microstructures after the high strain rate large strain plastic deformation processing by linear plane strain machining. This apparent lack of low-energy grain boundary segments and relatively high level of connectivity of weak links in the grain boundary network structure would likely be indicative of poor intergranular corrosion resistance.

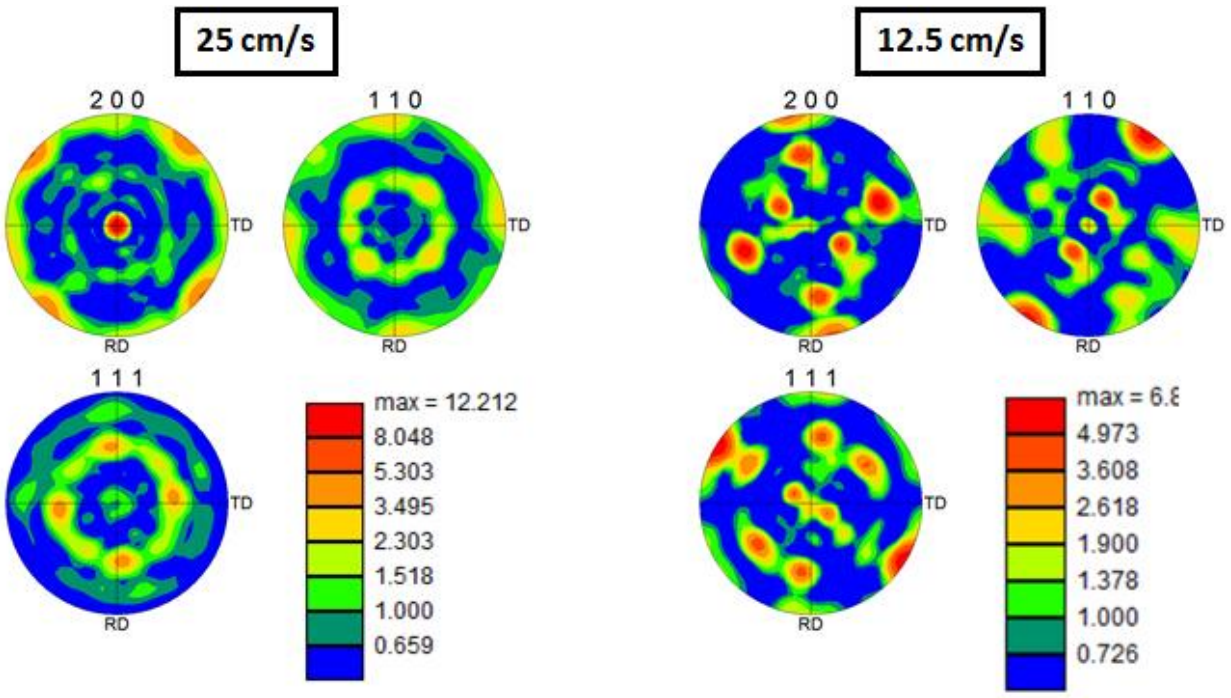

Figure 8 ï Texture representation by pole figures for two different velocities, 25cm/s and 12.5cm/s, of the 316L chip materials.

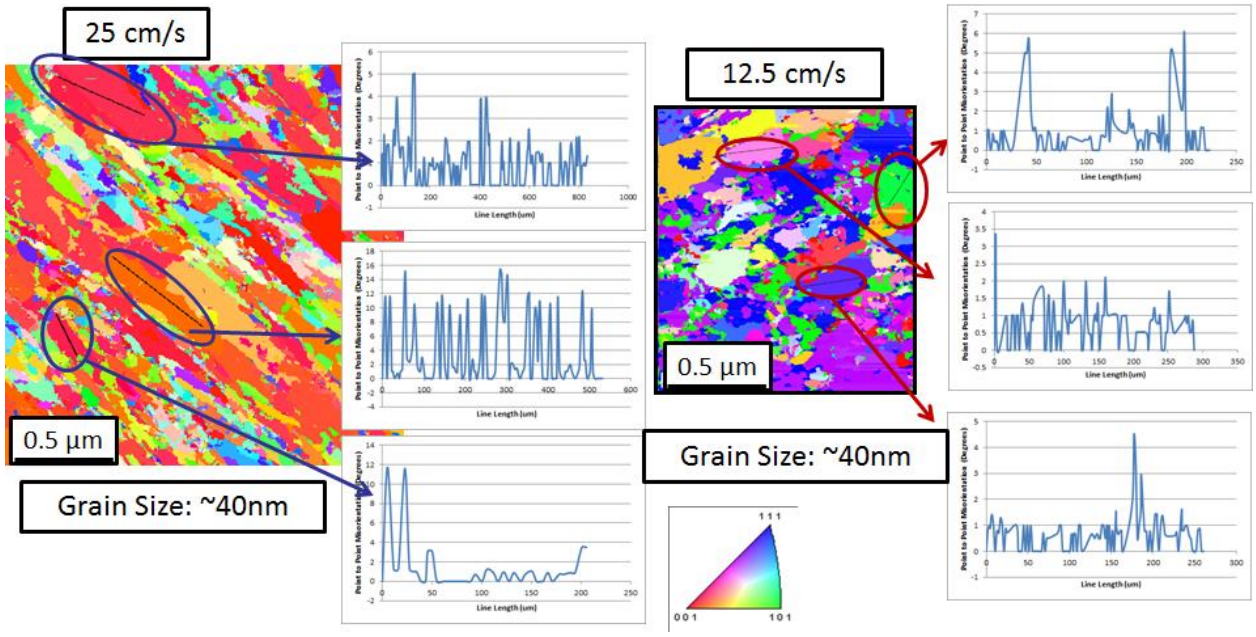

Figure 9 ï PED-OIM representations at two different velocities, 25cm/s and 12.5cm/s, showing the point-to-point disorientation for the chip materials.

Two different categories of observable trends can be stated regarding 2-D linear plane-strain machining of the 316L chips: tool velocity of 2.5 cm/s and tool velocities of above 6.25 cm/s where a change in deformation mechanism between the strain rates of 200 s^{-1} and 400 s^{-1} occurs. Below a strain rate of 200 s^{-1}, a larger fraction of strain induced martensite is present with moderate internal strain with a grain refinement to ~75 nm, which were obtained through DF analysis as shown in Table 5. Not only is determining the average grain size important, but understanding the grain size distribution is necessary to understand the microstructure. Figure 10 shows the grain size distribution for the slowest and highest tool velocity ï2.5 cm/s and 25 cm/s, which were associated with shear strain rate equivalents of about ~170 s^{-1} and ~1700 s^{-1}, respectively. All chip conditions show a grain size distribution where large grains exist (>200 nm) in the material even though most of the grains are significantly more scale refined (<100 nm). The 2.5 cm/s tool velocity condition shows a bi-modal distribution (one peak at ~25 nm and the other peak at ~ 85 nm). For all tool velocities above 2.5 cm/s, the grain size distribution becomes more compact and closer to unimodal. The 25 cm/s is shown in Figure 10 as an example of this characteristically close to or near unimodal distribution behavior (the major distribution peak is at ~20 nm). Because larger grains exist in the grain size distribution, the standard deviations are very large for the measured deformed chips. Above 400 s^{-1}, a consistent smaller fraction of strain-induced martensite (SIM) is present with moderate internal strain. As the strain rate is increased from 400 s^{-1} to ~1700 s^{-1}, the grains experience higher peak temperatures from the deformation process, the populations of grains shift from those with a high distribution of irregular shaped grains to those with more elongated shaped grains, and an increased sub-cell structure, as

noticed by the increase in intragranular strain and small angle grain boundaries. According to the PED-OIM maps, the grains appear to elongate and t o ñ p i n c h ing the micro- r a n s f o structure into a refined grain microstructure with a rough o r -ñt so a ograin boundary, in which the 25 cm/s is observed to have less rough grain boundary ï presumably due to a higher temperature change experience, which is related to the higher strain rate. These morphological characteristics of the grain boundaries are quite similar to those reported for geometric dynamic recrystallization (GDX), which is typically observed in hot rolling or friction welding deformation processes where temperatures are in excess of 900 €C [107]. GDX is defined as continuous recrystallization during high temperature deformation [108]. As the material is hot deformed, small angle grain boundary substructures are formed suppressing discontinuous recrystallization, which is inhomogeneous recrystallization [109]. Upon high strain and strain rates being applied, the steel is subjected to a large reduction in cross section, which is associated with the depth of cut from the linear plane-straining deformation process and thickness of resulting chip, and the original grains become flattened. Because the sub-grain size is not heavily dependent on the strain, the fraction of HAGBs increases significantly due to the influence of the strain rate causing the HAGBs to come closer to each other based on the sub-cell microstructure. The newly formed refined grain boundaries will develop a heavily serrated or roughened saw-tooth morphology where the scale of the serrations is based on the scale of the dislocation sub-cell microstructure [108]. Once the size of the serrated grain boundaries becomes comparable to the grain thickness, the serrated boundaries will come into contact. The boundaries are defects containing opposite signs causing annihilation of each other reducing the excess defect energy effectively inducing the grain pinch into two new grains [108]. As the strain rate is increased (here approximately doubled strain rate for the increase of 12.5 cm/s to 25 cm/s, e.g., it is obvious that

the grains have indeed become more flattened or more elongated. Also, with the increase in the strain rate the evolution of serrated grain boundaries is observed, while the average grain size remains nearly unchanged. Based on the definition of GDX, it appears this phenomenon is suitable to rationalize multiple microstructural features observed in the 2-D linear plane-strain machined 316L chips.

In summary, it is noted that the total strain imparted by the 2-D linear plane-strain machining deformation process is about the same for both the 12.5 cm/s and the 25 cm/s tool velocity conditions in the resulting chip; however, the strain rate for the 25 cm/s chip material is twice that for the 12.5cm/s chip material. Additionally, the grain size (~40 nm according to PED-OIM), MVF (~3%), and hardness (~500 VHN or tensile strength of ~1690 MPa) are similar; meanwhile, texture, grain shape, and grain boundary structure morphology is observable different (25 cm/s shows more elongated grains with more rough grain boundaries). It is hypothesized that the differences in the acquired data are a direct result of the strain rate differences and associated adiabatic process heating related differences in the chip microstructure for the chip material volumes in the center. This hypothesis is backed by temperature rise measurements in the chip revealing process related heating of the chip materials to be ~125°C and ~200°C for the 12.5 cm/s and 25 cm/s chip conditions respectively.

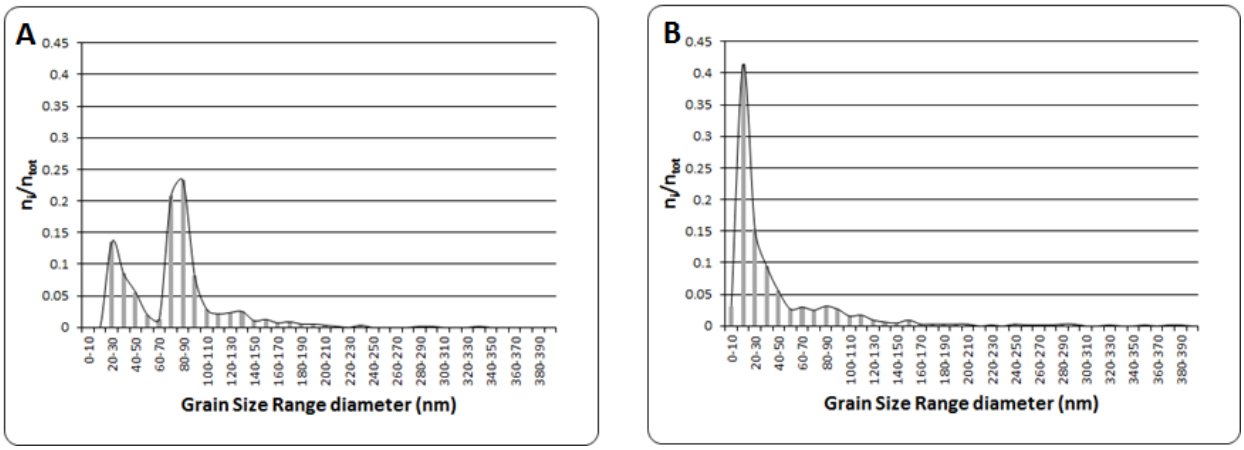

Figure 10 ïGrain size distribution for the as deformed 316L chips at (a) 2.5 cm/s and (b) 25 cm/s tool velocities as determined by DF analysis

4.2 SURFACE SUBSTRATE

In addition to producing the severely plastically deformed chips, the 2-D linear plane strain machining process also imparts plastic deformation and process heating to the surface regions of the bulk substrate. This section presents and discusses the effects of the plastic deformation processing by the plane-strain machining on the microstructures and properties of the bulk substrates obtained for the same conditions as the associated chip material volumes.

Figure **11** shows the XRD line scan obtained in plan-view geometry for the surface substrate following 2-D linear plane-strain machining with a tool velocity of 2.5 cm/s, 6.25 cm/s, 12.5 cm/s, and 25 cm/s. A very large martensite peak associated with the BCC {110} can be discerned in the 2.5 cm/s condition. For the other tool velocity conditions this BCC {110} peak, typical and characteristic of significant SIM formation, shows strongly reduced intensity. Utilizing the adjacent and strong {111} austenite and {110} martensite peaks for an intensity based martensite volume fraction (MVF) quantification provides a value of ~43% for the 2.5cm/s tool velocity processing condition, and about ~4%, ~ 3%, and ~1% for the 6.25 cm/s, 12.5 cm/s, and 25 cm/s tool velocity conditions, respectively. Notably, the maximum penetration depth of the X-rays used in the XRD studies here is limited to relatively small values of ~16 μm. Hence, these XRD based MVF data may indicate that the amount of the strain induced martensite created in the surface deformed area (approximately the top 16 μm) from the deformation process is a function of tool velocity. As tool velocity is decreased, the fraction of martensite formed in the surface deformed area increases significantly. Additionally, the effect of texture is very obvious

from the XRD line scans. The {200} and {220} austenite peaks cannot be detected for any of the four different velocity conditions. Qualitatively and quantitatively the texture evolution can be evaluated by observing the change in relative intensities of the I_{111}/I_{200} and I_{111}/I_{220} peaks in the deformed samples as compared to the as received material. The peak broadening analysis shows significant broadening for the {111} austenite peaks of 0.436°, 0.262°, 0.247°, and 0.227° for the chips produced with a tool velocity of 2.5 cm/s, 6.25 cm/s, 12.5 cm/s, and 25 cm/s respectively. Assuming the measured peak broadening observed for all conditions is associated entirely with non-uniform strain stored in the deformation processed microstructures, the strain magnitudes and elastic stress magnitudes are documented in Table 6. The strain and stress magnitudes indicate a significant amount of stored non-uniform strain in the 2.5 cm/s condition with a significant decrease in stored non-uniform strain in all other velocity conditions. These differences are consistent with the microstructural results observed in the chip materials. In the case where only grain size effects are considered in a peak broadening analysis of the {111} austenite peaks of the XRD data, the grain size for all tool velocity conditions are calculated as shown in Table 6. The error of measuring the respective peak widths results in an uncertainty of XRD based grain size of about ± 5 nm. This indicates that the differences between the 6.25 cm/s, 12.5 cm/s, and 25 cm/s tool velocity conditions are insignificant, ~35-40nm, while there is a significant and measurable decrease in XRD based grain size for the 2.5 cm/s tool velocity condition to ~20nm.

Figure 11 ïXRD line scan for the four different tool velocities of the surface substrate

Table 6 - Quantitative results of surface substrate d-at the 4 ness

Velocity (cm/s)	Microstrain	Stress (GPa)	Grain Size (nm) ïXRD	Hardness (VHN)	Tensile Strength (MPa)
As Received	-	-	~20000	159	~ 515
2.5	0.009 +/- 0.001	1.836 +/- 0.200	~20	356 +/- 19	~ 1150
6.25	0.005 +/- 0.001	1.104 +/-0.200	~35	294 +/- 13	~ 930
12.5	0.005 +/- 0.001	1.039 +/- 0.200	~35	358 +/- 12	~ 1150
25	0.005 +/- 0.001	0.955 +/- 0.200	~40	305 +/- 10	~ 960